The refertilized nature of the southern lithospheric mantle domain beneath the Massif Central (France): An example of xenoliths from Mt. Briançon

Malgorzata Ziobro-Mikrut, Jacek Puziewicz, Sonja Aulbach, Mary-Alix Kaczmarek, Franz Kiraly

LITHOS 482-483 (2024) 107670

Contents lists available at ScienceDirect

LITHOS

journal homepage: www.elsevier.com/locate/lithos

The refertilized nature of the southern lithospheric mantle domain beneath the Massif Central (France): An example of xenoliths from Mt. Briançon

Małgorzata Ziobro-Mikrut [a,*], Jacek Puziewicz [a], Sonja Aulbach [b], Mary-Alix Kaczmarek [c], Franz Kiraly [d]

[a] University of Wroclaw, Faculty of Earth Sciences and Environmental Management, Institute of Geological Sciences, Wroclaw, Poland
[b] Goethe University Frankfurt am Main, Institute for Geosciences and Frankfurt Isotope and Element Research Center (FIERCE), Frankfurt, Germany
[c] Géosciences Environnement Toulouse (GET), CNRS-CNES-IRD-Université Toulouse III, Observatoire Midi-Pyrénées, Toulouse, France
[d] University of Vienna, Department of Lithospheric Research, Vienna, Austria

ARTICLE INFO

Keywords:
Continental lithospheric mantle
Refertilization
MORB-melts
Xenoliths
Massif Central
France

ABSTRACT

Mantle xenoliths from the Cenozoic Mt. Briançon cinder cone in the Massif Central (France) were studied in order to test previously proposed hypotheses on the structure and chemical evolution of the lithospheric mantle in the region. Mineral major and trace element compositions coupled with characterization of crystal preferred orientation (CPO) of grains allow to recognize the compositional evolution and deformation history of peridotites and show which minerals constitute the primary vs. later fabric of the rock. The Mt. Briançon xenolith suite (n = 21) consists of spinel lherzolites, except one spinel harzburgite and one olivine clinopyroxenite. Lherzolites (olivine Fo 88.5–90.4) form three major groups. Those of Group I (51–65 vol% olivine and 10–16 vol% clinopyroxene) contain pyroxenes of variable Al content (orthopyroxene 0.142–0.217 apfu; clinopyroxene 0.244–0.316 apfu) and aluminous spinel (Cr# 0.09–0.12). Clinopyroxene is LREE-depleted and exhibits CPO indicating that it is a newly crystallized/recrystallized phase added to the rock framework consisting of olivine and orthopyroxene. Group II lherzolites (67–83 vol% olivine, 5–9 vol% clinopyroxene) contain Al-poor clinopyroxene (0.208–0.245 apfu) and spinel of Cr# 0.16–0.28. Clinopyroxene is LREE-enriched and its CPO is coherent with the fabric defined by olivine and orthopyroxene, indicating a joint deformation history. The lherzolites of Group Ia (46–66 vol% olivine, 11–26 vol% clinopyroxene) are transitional between those of Group I and II, and the majority contain pyroxenes with Al contents similar to those of Group I, and spinel of Cr# 0.11–0.15. Clinopyroxene REE patterns are spoon-shaped. Three lherzolites cannot be classified into the mentioned groups because they exhibit REE contents in clinopyroxene that change gradually from LREE-depleted to LREE-enriched on the scale of a petrographic section. In one of them, this change is observed at the grain scale, with spoon-shaped REE patterns in the cores and LREE-enriched ones at the margins. The harzburgite is rich in Mg (olivine Fo 91.1, pyroxenes Mg# 0.92) and impoverished in Al (spinel Cr# 0.43). Clinopyroxene is enriched in LREE, the contents of which are significantly lower than those of lherzolitic clinopyroxene. It forms nearly undeformed grains in an olivine-orthopyroxene framework. The lherzolites of Group I were formed by reactive percolation of MORB-like melts under suprasolidus conditions, which enabled replacement and/or addition of clinopyroxene to the solid olivine-orthopyroxene framework. Zonal REE distribution in clinopyroxene from one of the lherzolites documents alkaline melt percolation overprinting the Group I, which ultimately formed the Group II lherzolites. The lherzolites of Group Ia document transition between those of Group I and Group II. Hypothetical melt in equilibrium with clinopyroxene in olivine clinopyroxenite has a composition similar to that of the host lava. This rock likely represents a cumulate from the same melt that infiltrated the lithosphere during the Cenozoic volcanic activity of the Massif Central.

* Corresponding author at: Jagiellonian University, Institute of Geological Sciences, Kraków, Poland.
E-mail address: m.ziobro@uj.edu.pl (M. Ziobro-Mikrut).

https://doi.org/10.1016/j.lithos.2024.107670
Received 25 January 2024; Received in revised form 20 May 2024; Accepted 22 May 2024
Available online 29 May 2024

1. Introduction

A large area of Europe's basement was formed during the Variscan orogeny. While different units of the Variscan crust were recognized and described in detail (e.g. Franke et al., 2017; Schulmann et al., 2022), the underlying continental lithospheric mantle (CLM) has been seldom studied in relation to the crust-based division (e.g. Puziewicz et al., 2020). The CLM of the Variscan orogen in Europe has been sampled indirectly by alkaline lavas of the Central European Volcanic Province, which mark Cenozoic rifting in the foreland of the Alps (Dèzes et al., 2004), and more directly by mantle xenoliths contained therein.

Here, we describe a xenolith suite from Mt. Briançon in the Devès volcanic field (France) in order to characterize better the CLM underlying southern part of the French Massif Central. Although mantle xenoliths from this locality have been studied before (e.g. Harvey et al., 2010; Touron et al., 2008; Yoshikawa et al., 2010), the details of the combined microstructure, thermal and compositional evolution of the CLM beneath this locality remain to be unravelled. The mantle lithosphere beneath Mt. Briançon consists mostly of lherzolites resembling the depleted MORB mantle (DMM), and which contain LREE-depleted clinopyroxene. We show that these lherzolites originated by refertilization by MORB-like basaltic melts, consistent with the model suggested by Lenoir et al. (2000) and documented by Puziewicz et al. (2020) in xenolith suites from the nearby Allègre and Alleyras sites.

2. Geological setting

2.1. Cenozoic volcanism and Variscan crust of the French Massif Central

The xenoliths described in this study occur in lavas belonging to the Central European Volcanic Province (CEVP; Wimmenauer, 1974; Wilson and Downes, 2006). This consists of a large number of volcanic centres scattered on Variscan basement from SW Poland and W Czech Republic through Germany and France. The lavas are products of intraplate alkaline volcanic activity dated from Early Paleogene to recent (e.g. Wilson and Downes, 2006). This activity was connected with the uplift of Variscan basement blocks and development of a system of rifts (European Cenozoic Rift System – ECRIS) on the foreland of the Alpine orogen (Dèzes et al., 2004).

The Devès volcanic field was formed at ca. 3.5–0.5 Ma at the SE prolongation of the Limagne Graben (Fig. 1A). It consists mainly of nepheline-normative basanites forming lava flows, scoria cones and maars with tuffs (Woodland and Jugo, 2007). Mt. Briançon in the NW part of the Devès is a cinder cone with layers of pyroclastic material and massive scoria. There is no dating of those rocks and we assume their age is probably analogous to that of neighbouring lava flows, which occur close to Saint-Arcons-d'Allier (45° 03′ 54" N; 3° 33' 31" E) and were dated (K–Ar) at 0.6–2.7 Ma (Cantagrel and Prévot, 1971).

The Massif Central is a part of the Variscan orogen of Europe. The latter consists of a series of SE-dipping major lithotectonic units (e.g. Schulmann et al., 2022). Significant amounts of melt were dispersed in the middle- and lower crust underlying the orogen during late-orogenic collapse 305–295 Ma ago (Vanderhaeghe et al., 2020 and references therein). This enabled lateral movements and flattening of the orogenic root, producing a lower crust of uniform thickness and Moho located at a depth of 28–32 km, except of Cenozoic rift areas (Meier et al., 2016; Ziegler and Dèzes, 2006, and references therein). The Moho beneath the Massif Central is located at 28–29 km and is uplifted to ~24 km beneath the Limagne Graben (Zeyen et al., 1997), whereas the lithosphere-asthenosphere boundary (LAB) is located at 70–80 km (Granet et al., 1995).

2.2. Lithological variation of the lithospheric mantle beneath the Massif Central

The bulk rock study of peridotite xenoliths enabled Lenoir et al. (2000) to recognize two distinct mantle domains beneath the Massif Central to the north and south of latitude 45°30′ N. The northern domain is composed mainly of protogranular peridotites with pyroxene-spinel clusters. The peridotites are relatively depleted in incompatible major

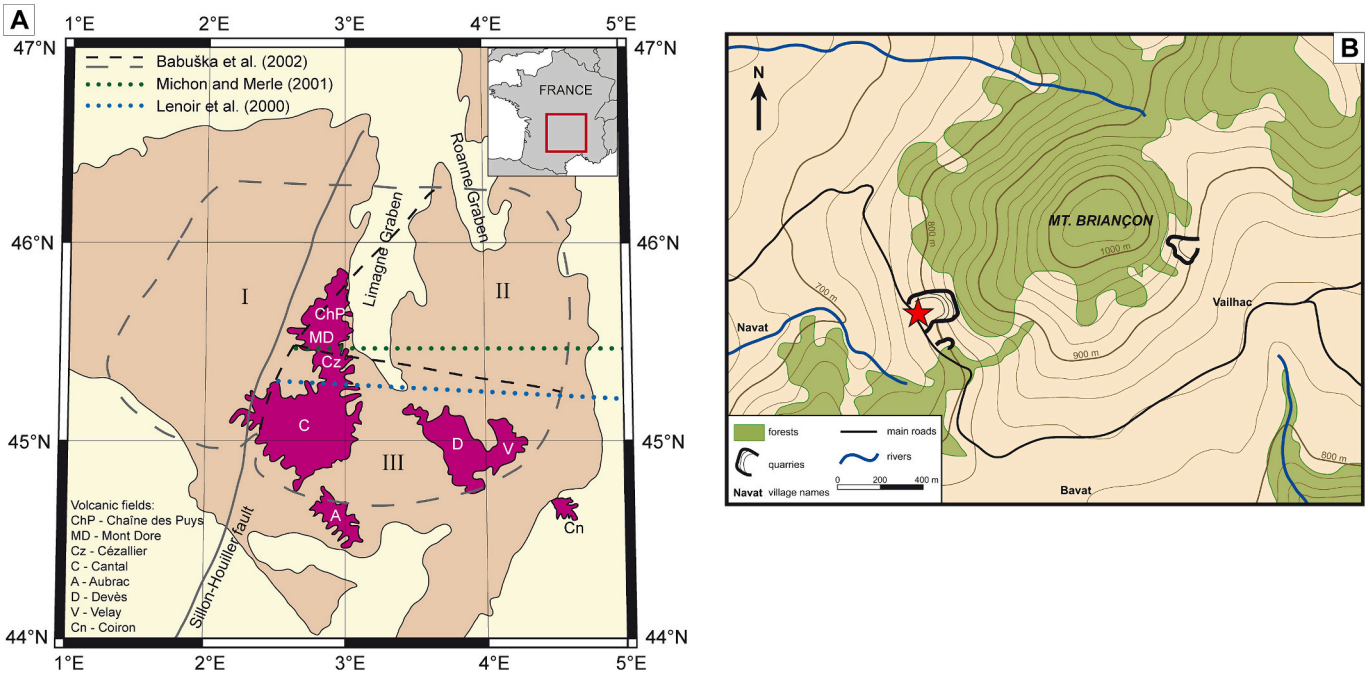

Fig. 1. A – Map illustrating locations of Cenozoic volcanics (violet) relative to Variscan basement of the Massif Central (light brown). I, II, III: seismic anisotropy domains recognized by Babuška et al. (2002), separated with black dashed lines. Green dotted line: boundary between volcanic domains after Michon and Merle (2001). Blue dotted line: boundary between lithospheric mantle domains after Lenoir et al. (2000). Map modified after Babuška et al. (2002). B – Topographic map of Mt. Briançon area, showing quarries and sampling locality (based on own field observations and Google Maps, 2023). (For interpretation of the references to colour in this figure legend, the reader is referred to the web version of this article.)

elements, but enriched in LREE and other incompatible trace elements. In contrast, peridotites of the southern domain do not contain pyroxene-spinel clusters, are dominantly coarse-granular and fertile in terms of major elements, but depleted in LREE. They resemble the depleted MORB mantle (DMM).

Uenver-Thiele et al. (2017 and references therein) indicated that the boundary between the domains is located slightly to the south (45°20′ N) of that suggested by Lenoir et al. (2000). It corresponds approximately (Fig. 1A) to the division of northern and southern volcanic areas of Michon and Merle (2001) and with the geophysically-defined northern and southern part of the eastern mantle anisotropy domains defined by Babuška et al. (2002).

Lenoir et al. (2000) interpret their observations as evidence that the lithosphere beneath the Massif Central is composed of two distinct blocks. The northern one could be a remnant of pre-Variscan lithosphere incorporated into the Variscan orogen. The southern block was probably rejuvenated during the Variscan orogeny. Downes et al. (2003) drew similar conclusions based on in-situ trace element and Nd–Sr isotope analyses of clinopyroxene separates.

Uenver-Thiele et al. (2017 and references therein) showed that the main metasomatic agents operating in the Massif Central lithospheric mantle were subduction related fluids (only in the northern domain), silicate and locally carbonatite and carbonated-silicate melts.

Puziewicz et al. (2020) combined geochemical and microstructural studies on xenoliths from the southern domain. They concluded that LREE-depleted clinopyroxene is texturally later than the olivine-orthopyroxene fabric and thus it is of metasomatic origin. To explain this, the authors proposed that originally harzburgitic mantle of the southern domain was pervasively modified by MORB-type melts derived from large-scale melting of upwelling asthenosphere in a process similar to that described by Le Roux et al. (2007) for the Lherz massif in Pyrenees.

The mantle xenoliths from Mt. Briançon were studied by Harvey et al. (2010), Touron et al. (2008), Yoshikawa et al. (2010), applying analytical techniques similar to those used in the present study (electron microprobe and LA-ICP-MS). All these studies show that clinopyroxene is LREE-depleted but Al-rich. Harvey et al. (2010) suggest a $\geq$ 1.8 Ga model Re depletion age of the Mt. Briançon xenoliths. Touron et al. (2008) suggest that Mt. Briançon xenoliths record low degrees (<5%) of melt extraction. Yoshikawa et al. (2010) conclude that melt extraction was followed by metasomatism by asthenosphere-derived melts.

3. Analytical methods and terminology

3.1. Sampling and methodological approach

We collected 137 xenoliths from the main quarry on Mt. Briançon (Fig. 1B). We selected 32 unweathered xenoliths representing the macroscopically recognizable petrological variability of the suite to make petrographic thick sections (100 μm). In the majority of hand specimens, neither foliation nor lineation was visible and thus the xenoliths were cut randomly. Some samples were cut perpendicularly to the weakly visible foliation defined by shape-preferred orientation of olivine and pyroxene grains, whereas the lineation was unclear. After preliminary observations under the optical microscope and scanning electron microscope (SEM) 21 samples have been chosen for a detailed petrographic and geochemical study.

Modal compositions of analysed samples were determined using the JMicroVision software (Roduit, 2007) by point counting on a random grid, which have been compared to electron backscatter diffraction (EBSD) phase maps. We used high resolution optical images of the sections or elemental maps and counted 300–400 points. The elemental maps were made using Jeol JSM-100 SEM and the Aztec software.

In-situ chemical analyses of all selected sections have been done with electron microprobe (Electron Probe Microanalysis, EPMA) for major elements and laser ablation inductively coupled plasma mass spectrometer (LA-ICP-MS) for trace elements. The EBSD technique was used to determine the crystal-preferred orientation (CPO) of minerals in 10 sections.

3.2. Electron microprobe analyses

We analysed major element compositions of olivine, orthopyroxene, clinopyroxene and spinel grains using a Cameca SXFiveFE at the Department für Lithosphärenforschung of University of Vienna, Austria. Standard conditions were applied: accelerating voltage of 15 kV, probe current of 15 nA, counting times of 10 s (background) and 20 s (peak), PAP correction, and natural silicates and synthetic oxides as standards. To improve detection limits of Ca and Ni in olivine we extended counting times for those elements to 30 s on background and 60 s on peak. We analysed 5–8 grains of each mineral per thick section. For each grain at least two analyses were made: one in the centre of the grain (termed "core") and one close to the margin (termed "rim") to recognize possible intra-sample and intra-grain variations in major elements compositions. In larger grains, 3 or 4 analyses were made from the centre towards the margin. The results and detection limits are reported in Appendix A.

Atomic ratios of elements were calculated from microprobe analyses on a basis of 4 (olivine) and 6 (pyroxenes) atoms of oxygen or 3 cations (spinel) and given in atoms per formula unit (apfu). For spinel, the proportion of Fe^{2+} and Fe^{3+} was calculated by charge balance (after Droop, 1987).

3.3. LA-ICP-MS analyses

Trace element compositions of ortho- and clinopyroxene grains were analysed in situ using a M-50 HR Resonetics laser ablation system (with a 193 nm ArF Excimer Laser) coupled with a Thermo Scientific ELEMENT XR ICP-MS at the Institut für Geowissenschaften of Goethe University in Frankfurt am Main, Germany, housed by the Frankfurt Isotope and Element Research Center (FIERCE). We used the following parameters: laser energy of 100 mJ, repetition rate of 8 Hz, spot diameter of 60 μm for clinopyroxene and 72 μm for orthopyroxene, resulting in an energy on the sample of ~3 J/cm^2. The NIST612 glass was used in each run for sensitivity calibration. Secondary standards of BIR-1G and BCR-2G (basalt glasses) were used to assess accuracy, which is on average better than 6% for all elements except Pb (12%) and precision (Appendix B). In addition, San Carlos orthopyroxene was analysed repeatedly to monitor precision. For NIST612, reference values after Jochum et al. (2011) were used. The internal standards were average SiO_2 contents in ortho- and clinopyroxene from each sample, measured by the electron microprobe. In each section, we analysed 3–5 grains per mineral with 1–2 spots per grain.

The data were processed using the Glitter 4.0 software (van Achterberg et al., 2001). We calculated relative standard deviation (rSD) for each element to assess homogeneity. Relative standard deviation is a standard deviation of particular element's concentration in a sample, divided by an average concentration of this element in the sample. We assumed that rSD $\leq$20% points to relatively homogenous distribution of an element in a sample which allows us to use its average concentration. For clinopyroxene in majority of samples rSD for most of trace elements is $\leq$10% (Appendix B). In case of highly incompatible elements (Rb, Ba, U, Th, Nb, Ta) higher rSD values are taken to reflect low concentrations of those elements and analysis near the detection limit, rather than geological variability in the sample. This may be also the case for LREE concentrations in orthopyroxene which are typically low. Higher variability of measured REE contents in orthopyroxene may be also caused by the presence of small portions of clinopyroxene located deeper inside a grain and thus impossible to see under the optical microscope or SEM. All the results together with average and rSD values are reported in Appendix B. For the figures the REE and trace elements concentrations were normalized to primitive mantle (PM) after McDonough and Sun

(1995).

3.4. Electron backscatter diffraction

Crystallographic preferred orientations were measured in 9 lherzolites (4001, 4006, 4008, 4009, 4013, 4015, 4024, 4027, 4031) and one harzburgite (4025). Mechanic-chemical polishing using a Vibromet (Buehler) was applied to thick sections for approximately 1 hour 30 minutes with a colloidal silica suspension (pH 10) to remove mechanically induced surface damage. EBSD data acquisition was performed with a JEOL 7100 microscope at the centre of microcharacterisation Raimond Castaing (University Paul Sabatier, Toulouse, France), equipped with an EBSD camera CMOS Symmetry S2 (Oxford Instruments). The analyses were performed with an acceleration voltage of 20 kV, a probe current of 16 nA, a working distance of 17 or 26 mm with a stage tilt of 70°, and a step size of 25 μm. Automatic indexing was performed using AZTec software (version 6.0 Oxford Instruments). The resulting EBSD data were processed in Flamenco software-channel 5. The data were noise-reduced using a "wildspike" correction to remove isolated erroneous points. This step was followed by a zero solution extrapolation up to six-neighbour following standard procedures proposed by Prior et al. (2002) and Bestmann and Prior (2003). At each of these steps, the resulting orientation maps were compared with band contrast maps to ensure that the data treatment did not compromise the data. The grains are identified by grains boundaries higher than 10°. Pole figures were plotted on a lower-hemisphere, equal-area stereographic projection. To avoid oversampling of large crystals, pole figures were plotted with one point per grain. For clarity and to compare easily the samples, pole figures were rotated as the inferred foliation was the XY plane (with olivine [010] point maxima normal to the foliation) and as the inferred lineation parallel to X highlight the correlation between the crystallographic axes of olivine [100] parallel to orthopyroxene and clinopyroxene [001] axes.

3.5. Geothermometry

Two geothermometers (Brey and Köhler, 1990; Liang et al., 2013) have been used in this study, based on major- and trace element chemical compositions of ortho- and clinopyroxene. We chose pyroxenes for temperature calculations because: (1) it is relatively easy to determine their textural position relative to olivine and spinel and (2) the abovementioned geothermometers are calibrated for a wide range of pyroxenes and host peridotite compositions. Applying two methods based on elements with different diffusion rates allows to recognize episodes of cooling or heating possibly recorded in xenoliths, as closure temperatures for trivalent elements in pyroxenes are higher than those for divalent elements (e.g. Liang et al., 2013).

The geothermometer of Brey and Köhler (1990) allows to calculate the temperature (T_{BKN}) at which the exchange of major elements between the adjacent ortho- and clinopyroxene grains stopped. The input data are concentrations of Mg, Fe, Ca and Na measured by electron microprobe and calculated to atomic ratios per formula unit. We calculated temperatures for 4–7 pairs of pyroxene per sample. For each ortho-clinopyroxene pair, we calculated one temperature based on analyses from cores and one based on analyses from rims. The assumed pressure was 1.5 GPa which is considered a typical value for spinel peridotite facies. We found that 5 samples give systematically higher results in rims than in cores, and we report ranges of T_{BKN} separately for cores and rims. The method's error is 30 °C (±15 °C) and adding 10 °C to consider analytical uncertainties, we assumed that differences ≤40 °C between the minimum and maximum T_{BKN} value in a sample mean that the pyroxenes are in chemical equilibrium in the studied rock sample. Conversely, the variation of calculated temperatures >40 °C at the scale of petrographic section suggests lack of chemical equilibrium among pyroxene grains at the scale of millimetres.

The geothermometer of Liang et al. (2013) is based on average REE contents in ortho- and clinopyroxene from a given sample, yielding a single value per xenolith (T_{REE}). For sample 4023 with highly heterogeneous REE compositions we also calculated a set of T_{REE}s based on pairs of single analyses of pyroxene cores and rims (Appendix C). Additionally, the spreadsheet provided by Liang et al. (2013) calculates "average" T_{BKN} using mean major element compositions of pyroxenes from a sample (here termed L-T_{BKN}). Apart from this, major elements compositions are also used to calculate several coefficients necessary to obtain partition coefficients of REE between ortho- and clinopyroxene in a given sample. Knowing from T_{BKN} calculations based on pairs of single analyses (previous paragraph) that several samples are not in equilibrium in terms of major elements, we excluded those samples from T_{REE} calculations. To evaluate REE equilibrium, we used diagrams of distribution of REE concentrations between orthopyroxene and clinopyroxene as a function of trivalent cationic radius in VIII-fold coordination (Agranier and Lee, 2007). All samples used for T_{REE} plotted along lines denoting REE equilibrium between those phases (Appendix D). Also, to ensure robustness of the calculated T_{REE}, we used only the elements with rSD ≤20% in the Liang et al. (2013) spreadsheet.

The presented approach yields 3 temperatures (T_{BKN}, L-T_{BKN}, T_{REE}). To avoid using three similar values in such cases, we decided to calculate a mean temperature for each sample in which T_{BKN} averaged from pairs of single analyses, T_{REE} and "average" T_{BKN} from the T_{REE} spreadsheet (L-T_{BKN}) differ <40 °C. We consider those mean temperatures as representative for the mentioned samples and we will use them in the discussion section. For the rest of the samples, we discuss T_{BKN} and T_{REE} separately, including differences for cores and rims revealed by T_{BKN}.

3.6. Terminology

In this paper, we use nomenclature for peridotite textures as proposed by Mercier and Nicolas (1975). Additionally, we use two descriptive terms in order to avoid genetic interpretations: "serial texture" defined by a gradual change of grain diameters from the smallest ones to the largest ones and "mosaic texture" defined by lobate boundaries of mineral grains constituting the rock. The textural position of mineral phases is described as follows: I – primary mineral grains; II – lamellae in pyroxenes; IIIa – mineral phases forming reaction rims around primary grains; IIIb – mineral phases forming fine-grained interstitial aggregates (Fig. 2; Matusiak-Małek et al., 2014; Puziewicz et al., 2023). "Fo" stands for forsterite content in olivine, denoting atomic ratio 100·Mg/(Fe^{total} + Mg + Mn) given in percent. Mg-number

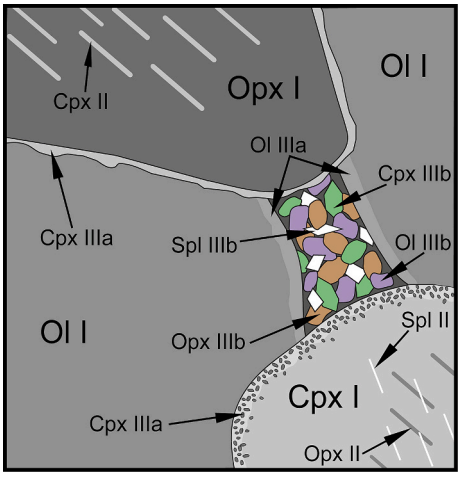

Fig. 2. Sketch illustrating the classification of minerals according to their textural position in mantle peridotite. I – primary mineral grains; II – lamellae in pyroxenes; IIIa – minerals forming reaction rims around primary grains; IIIb – minerals forming fine-grained interstitial aggregates. Modified after Puziewicz et al. (2023) and Tedonkenfack et al. (2021).

(Mg#) stands for atomic Mg/(Mg + Fe^{total}) for pyroxenes and for Mg/(Mg + Fe^{2+}) for spinel. Cr-number (Cr#) stands for atomic Cr/(Cr + Al) for spinel. Mineral abbreviations are as follows: Ol (olivine), Opx (orthopyroxene), Cpx (clinopyroxene), Px (pyroxenes), Spl (spinel).

4. Petrography and mineral chemistry

4.1. Petrography

The Mt. Briançon xenoliths are 4–14 cm in diameter, with oval to subangular shapes. The suite consists of spinel-facies peridotites: 19 lherzolites and a single harzburgite (Fig. 3). One xenolith consists dominantly of lherzolite, occurring in contact with pyroxenite, the two showing a diffuse boundary (Fig. 4A). The latter consists of orthopyroxene, clinopyroxene and spinel, but its small volume does not allow to determine the exact modal composition. We also found another composite xenolith, consisting of olivine clinopyroxenite with small portions of peridotite at the edges (Fig. 4B).

The main classification of the xenoliths we use in the text is based on their lithology. The lherzolites are the most abundant lithology in the investigated suite and they have diverse chemical characteristics. Thus, we further divide them into three groups based on REE contents in clinopyroxene, which will be described in the Section 4.3.1. Additionally, there are three lherzolites that are described separately because they fall beyond this division, as their clinopyroxene REE contents are not homogeneous at the scale of the sample (see Section 4.3.2).

The harzburgite and the majority of lherzolites have variably developed porphyroclastic texture (Fig. 4A,C,E, Table 1). In most cases, the porphyroclasts are olivine (2.2–4.5 mm in diameter) and/or orthopyroxene (1.5–3.4 mm). Some xenoliths contain also clinopyroxene porphyroclasts (1.3–2.1 mm in diameter, Table 1). Seven lherzolites exhibit serial texture (Fig. 4D, Table 1) with grain diameters changing continuously from 0.3 mm to 2.5 mm (olivine, orthopyroxene) or to 1.6 mm (clinopyroxene). In harzburgite and all lherzolites, orthopyroxene grains are clear, with no optically visible lamellae or spongy rims. Scarce clinopyroxene grains have spongy rims or spinel/orthopyroxene lamellae (Table 1). Spinel grains occur in different shapes: roughly isometric, amoeboidal or elongated (Fig. 4C, D, F).

In thick sections, most of the lherzolites exhibit weak foliation defined by shape-preferred orientation of part of olivine and/or orthopyroxene grains. Foliation in lherzolite 4005 is underlined by streaks of spinel grains (Fig. 4F). Lherzolites 4020, 4023 and harzburgite 4025 exhibit elongation of spinel-pyroxene clusters or preferred orientation of elongated spinel grains (Table 1).

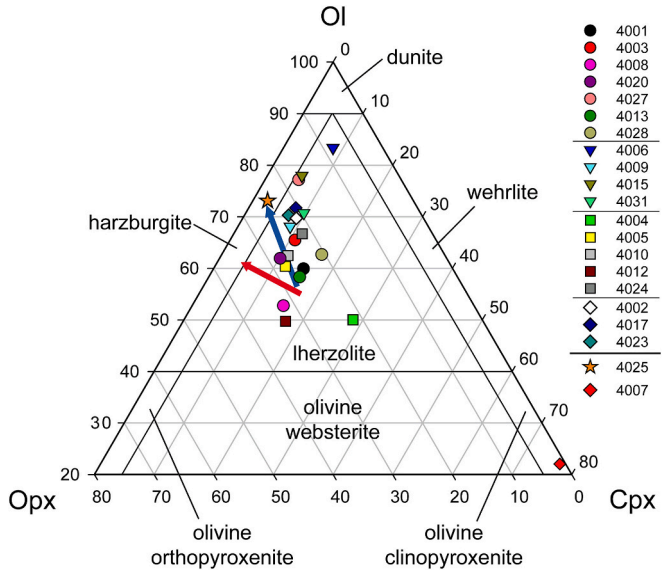

Fig. 3. Mineralogical classification of Mt. Briançon xenoliths in the Ol-Opx-Cpx diagram of the IUGS (Streckeisen, 1976). The arrows show isobaric melting paths determined experimentally at 1 GPa (blue) and 2 GPa (red), data after Niu et al. (1997). (For interpretation of the references to colour in this figure legend, the reader is referred to the web version of this article.)

Lherzolite 4006 contains a pyroxenite layer formed by orthopyroxene, clinopyroxene and spinel (Fig. 4A). The olivine clinopyroxenite (sample 4007) consists of clinopyroxene grains with diameters changing gradually from 0.2 to 2 mm and smaller (0.3–0.9 mm) olivine grains. The boundaries of the grains are lobate, forming a mosaic texture (Fig. 4B).

4.2. Crystallographic preferred orientation

Olivine in harzburgite and all lherzolites exhibits CPO with point concentrations on [100] axes that are parallel to X (Fig. 5). Point concentrations on [010] axes are parallel or sub-parallel to Z, except for lherzolite 4001 containing olivine with scattered [010] axes and point concentration on [001] axes parallel to Z. Olivine [001] axes in lherzolites 4009 and 4015 show a point concentration parallel to Y and in lherzolite 4024 and harzburgite 4025 display a weaker concentration parallel to Y. All studied samples contain olivine with CPO suggesting the activation of [100](010) type-A slip-system, except lherzolite 4001 with a CPO showing a [100](001) type-E slip-system (slip-systems defined by Jung and Karato, 2001; Katayama et al., 2004).

In most of the lherzolites, orthopyroxene [001] axes show point concentrations which are parallel or sub-parallel to X and to olivine [100] axes (Fig. 5). In contrast, in lherzolites 4006, 4013 and harzburgite 4025 orthopyroxene [001] axes are at high angle (from 45°) to olivine [100] axes. In lherzolite 4001, orthopyroxene [001] axes are at slight angle to olivine [100] axes, but in the foliation plane (XY).

Olivine and orthopyroxene crystallographic orientations define the fabric of lherzolites and the harzburgite, and clinopyroxene crystallographic orientations are either coherent with olivine and orthopyroxene or not. Lherzolites 4027, 4009, 4015, 4031 and 4024 contain clinopyroxene with [001] axes parallel or at slight angle (<45° in sample 4027) to X, to olivine [100] and orthopyroxene [001] axes (Fig. 5). Clinopyroxene in harzburgite 4025 display a slight concentration of [001] axes within a girdle in the foliation plane (XY). Lherzolites 4001, 4006, 4008, 4013 have scattered clinopyroxene [001] axes.

In the pyroxenitic part of sample 4006, orthopyroxene CPO are scattered but [100] axes mimic the orthopyroxene CPO from the lherzolitic part (Fig. 5). The clinopyroxene CPO in the pyroxenite layer display [001] axes at low angle to olivine [100] axes from the lherzolite.

4.3. Mineral chemistry

4.3.1. Lherzolites with homogeneous mineral chemical composition

Olivine I occurring in lherzolites contains 88.5 to 90.4% Fo, 0.38–0.41 wt% NiO and 260–600 μg/g Ca (Fig. 6A-B, Table 2). It is homogeneous at the sample scale (Appendix A). The exceptions are lherzolites 4002 and 4023, which contain olivine with broader range of Fo. Orthopyroxene (Mg# 0.89–0.91) contains 0.13–0.22 Al atoms pfu (Fig. 6C), whereas clinopyroxene (Mg# 0.88–0.91) contains from 0.20 to 0.32 Al atoms pfu (Fig. 6D). Spinel has Cr# ranging from 0.09 to 0.28 (Fig. 6E). Points showing the relationship among olivine Fo and spinel Cr# (Fig. 6F) fall in the Olivine-Spinel Mantle Array of Arai (1994).

We classify the lherzolites into 3 groups based on the REE patterns of clinopyroxene I (Fig. 7, Table 2, Appendix B). Group I is defined by the occurrence of clinopyroxene with REE patterns that are relatively flat from Lu to Eu and depleted in lighter REE, and comprises lherzolites 4001, 4003, 4008, 4013, 4020, 4027, 4028. Orthopyroxene REE patterns exhibit a relatively steep decrease in normalized element concentrations from Lu to La, defining Group I orthopyroxene (Appendix E).

Group II comprises lherzolites 4006, 4009, 4015, 4031, containing clinopyroxene with REE patterns that are variably enriched in LREE

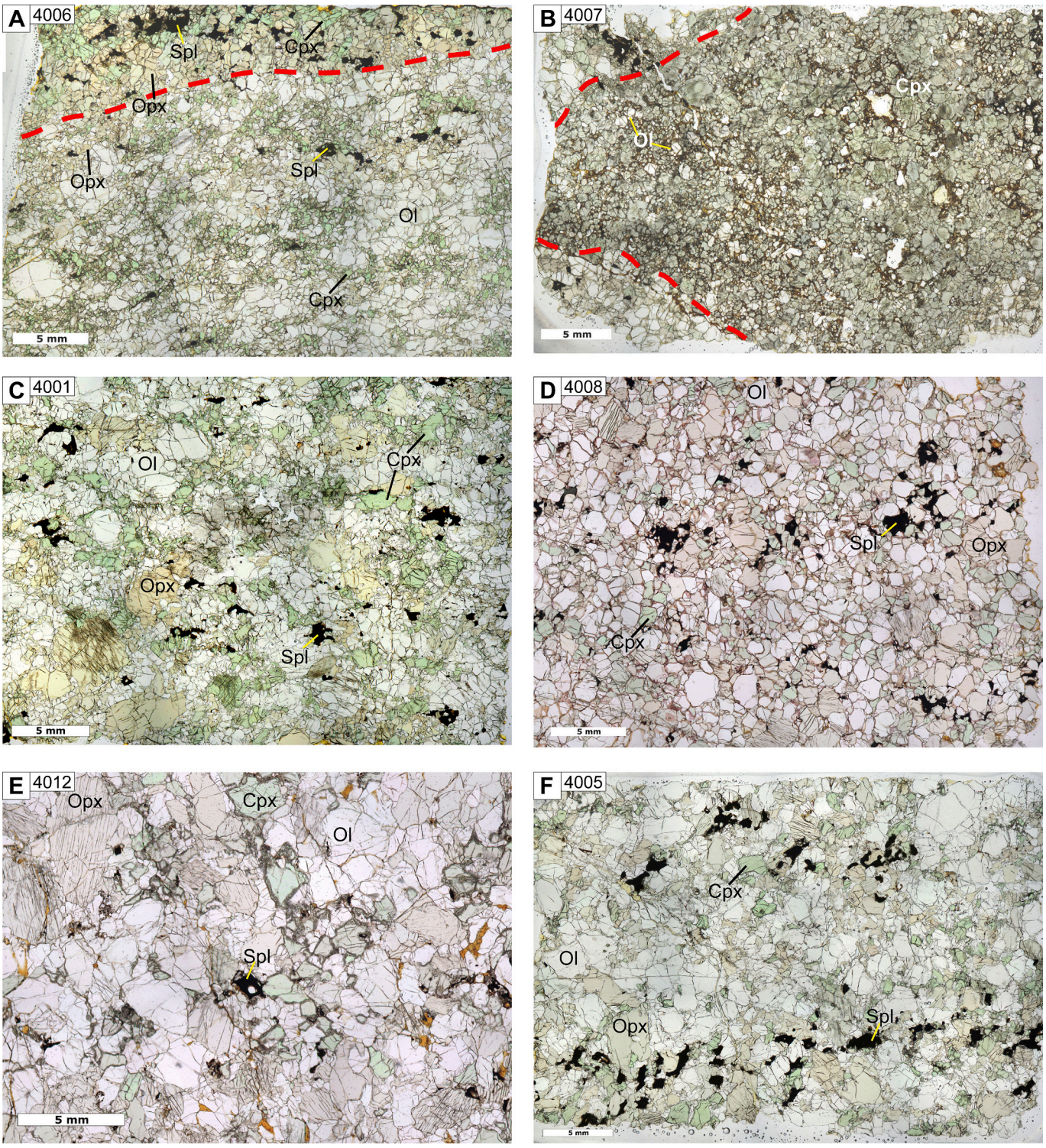

Fig. 4. Petrography of Mt. Briançon xenoliths. A, C, E – variably developed porphyroclastic texture. A – composite xenolith dominated by lherzolite with pyroxenite layer at its upper edge. B – composite xenolith dominated by olivine clinopyroxenite with peridotite at the top and bottom left edges. D – equigranular to serial texture in lherzolite. F – foliation defined by slight elongation of a part of the olivine grains, underlined by streaks of spinel grains in porphyroclastic lherzolite. All images are transmitted-light microphotographs.

relative to HREE (Fig. 7, Table 2). Orthopyroxene REE patterns are moderately depleted in LREE relative to HREE, defining Group II orthopyroxene (Appendix E). Orthopyroxene in lherzolite 4031 exhibits a REE pattern that is moderately depleted from Lu to Gd and relatively flat from Gd to La. The REE patterns of clinopyroxene and orthopyroxene from lherzolite 4006 exhibit the same shapes as REE patterns of those phases from the pyroxenite layer.

Clinopyroxene in lherzolites 4004, 4005, 4010, 4012, 4024 has spoon-like REE patterns which are transitional between those of Group I and II, and we classify them as Group Ia (Fig. 7). Orthopyroxene in those lherzolites exhibits REE patterns from highly to moderately depleted in LREE relative to HREE (Appendix E).

Table 1
Summary of petrographic observations on xenoliths from Mt. Briançon.

Sample name	Longest dimension [cm]	Modal composition [vol%]				Lithology	Texture	Lamellae		Spongy rims		Other features
		Ol	Opx	Cpx	Spl			in Opx	in Cpx	in Cpx	in Spl	
4001	9.5	59.0	24.5	15.1	1.4	lherzolite	porphyroclastic			+	+	Spl partially interstitial
4003	7.0	65.0	23.3	10.6	1.1	lherzolite	serial		+			lamellae in Cpx, Opx, Spl
4008	12.0	51.3	31.4	14.7	2.6	lherzolite	serial					amoeboidal or interstitial Spl
4013	7.5	56.5	25.5	15.2	2.8	lherzolite	serial			+	+	fine-grained Ol-Cpx-glass aggregates around amoeboidal Spl
4020	5.5	61.6	27.7	10.0	0.7	lherzolite	porphyroclastic Ol, Opx				+	preferred elongation of Spl grains
4027	5.5	75.3	17.8	5.3	1.6	lherzolite	serial			+	+	amoeboidal Spl
4028	10.0	60.3	19.7	16.0	4.0	lherzolite	serial				+	
4006	9.0	83.8	8.1	7.8	0.3	lherzolite + pyroxenite	porphyroclastic Ol					fine-grained Ol-Cpx-Spl aggregates around some Spl grains
4009	14.0	67.6	22.7	8.3	1.4	lherzolite	porphyroclastic Ol, Opx			+	+++	fine-grained Ol-Cpx-glass aggregates around Spl grains
4015	6.5	76.3	17.5	5.5	0.7	lherzolite	porphyroclastic Ol, Opx		+ Spl		+	fine-grained Ol-Cpx aggregates around some Spl grains
4031	7.5	67.0	18.7	9.3	5.0	lherzolite	porphyroclastic Ol, Opx			+	++	fine-grained Ol-Cpx-glass aggregates around Spl grains
4004	8.0	46.1	20.1	26.3	7.5	lherzolite	porphyroclastic		++ Spl		+	Spl partially interstitial
4005	8.5	56.7	26.0	11.0	6.3	lherzolite	porphyroclastic Ol, Opx			++	++	interstitial Spl arranged in streaks, surrounded by fine-grained Ol-Cpx-glass aggregates
4010	10.5	62.0	26.0	11.0	1.0	lherzolite	porphyroclastic Ol, Opx			+	+++	Spl surrounded by porous glass
4012	9.0	49.0	33.0	17.0	1.0	lherzolite	porphyroclastic with protogranular relics			+++	++	some fine-grained Ol-Cpx aggregates; Cpx partially interstitial
4024	7.0	66.0	21.3	11.3	1.4	lherzolite	porphyroclastic Opx			+	+	
4002	8.0	68.0	20.6	8.7	2.7	lherzolite	porphyroclastic				+	Spl partially interstitial
4017	8.0	70.6	20	7.7	1.7	lherzolite	serial				+	
4023	4.0	68.3	22.0	6.7	3.0	lherzolite	serial		++ Spl		+	Spl arranged in streak; fine-grained Ol-Cpx aggregates around some Spl grains
4025	6.0	72.9	23.0	3.5	0.6	harzburgite	porphyroclastic Opx					preferred elongation of Spl grains
4007	5.5	22.0	1.0	77.0	0.0	olivine clinopyroxenite + peridotite	mosaic			++		several grains of Ca carbonates

The peridotites are grouped according to groups defined by REE contents in clinopyroxene (see Section 4.3 for explanations). For composite xenoliths (4006 and 4007) modal composition of the dominant lithology is shown (see Section 4.1 for explanations). Mineral abbreviations in "Texture" column indicate which phases form porphyroclasts. If no abbreviations are present, the porphyroclasts are Ol, Opx, Cpx. Occurrence of lamellae and spongy rims: + in some grains, ++ in majority of grains, +++ in all grains.

4.3.2. *Lherzolites with heterogeneous mineral chemical composition*

Lherzolites 4002 and 4023 exhibit greater variation of Mg# in all silicate phases than the rest of the rocks (Fig. 6, Appendix A). In 4002, olivine Fo content varies from 86.4 to 89.3%, orthopyroxene Mg# is 0.87–0.90 and clinopyroxene Mg# is 0.86–0.89. These changes occur gradually across the thick section (Fig. 8). The REE contents and patterns are homogeneous at the grain scale, but vary across the thick section from spoon-shaped to slightly LREE-enriched (Fig. 8). Orthopyroxene is significantly depleted in LREE relative to HREE (Appendix E).

In lherzolite 4023, olivine contains 88.8–90.2% Fo, and Mg# of pyroxenes is 0.89–0.91. The olivine Fo and orthopyroxene Mg# gradually change perpendicularly to the foliation defined by elongation of spinel-pyroxene cluster (Fig. 8), whereas clinopyroxene grains with various Mg# are randomly distributed. The cores of clinopyroxene exhibit spoon-like to LREE-enriched patterns, whereas the rims are exclusively LREE-enriched. (Fig. 8). Orthopyroxene is moderately depleted in LREE relative to HREE (Appendix E).

Lherzolite 4017 contains minerals whose major element chemical compositions are homogeneous. Clinopyroxene exhibits spoon-like REE patterns with variation of LREE among the grains. The majority of grains have similar REE patterns in core and rim, with rims slightly enriched in LREE. One grain in area 4 is an exception, with a rim that exhibits significantly higher LREE enrichment than the core (Appendix F). Orthopyroxene REE patterns are mildly depleted in LREE relative to HREE (Appendix E).

4.3.3. *Harzburgite*

Harzburgite 4025 contains olivine Fo 91.1%, 0.41 wt% NiO and 510–670 μg/g Ca (Fig. 6, Table 2). Pyroxenes have Mg# 0.92 and contain 0.11 atoms of Al pfu (orthopyroxene) and 0.14 atoms Al pfu

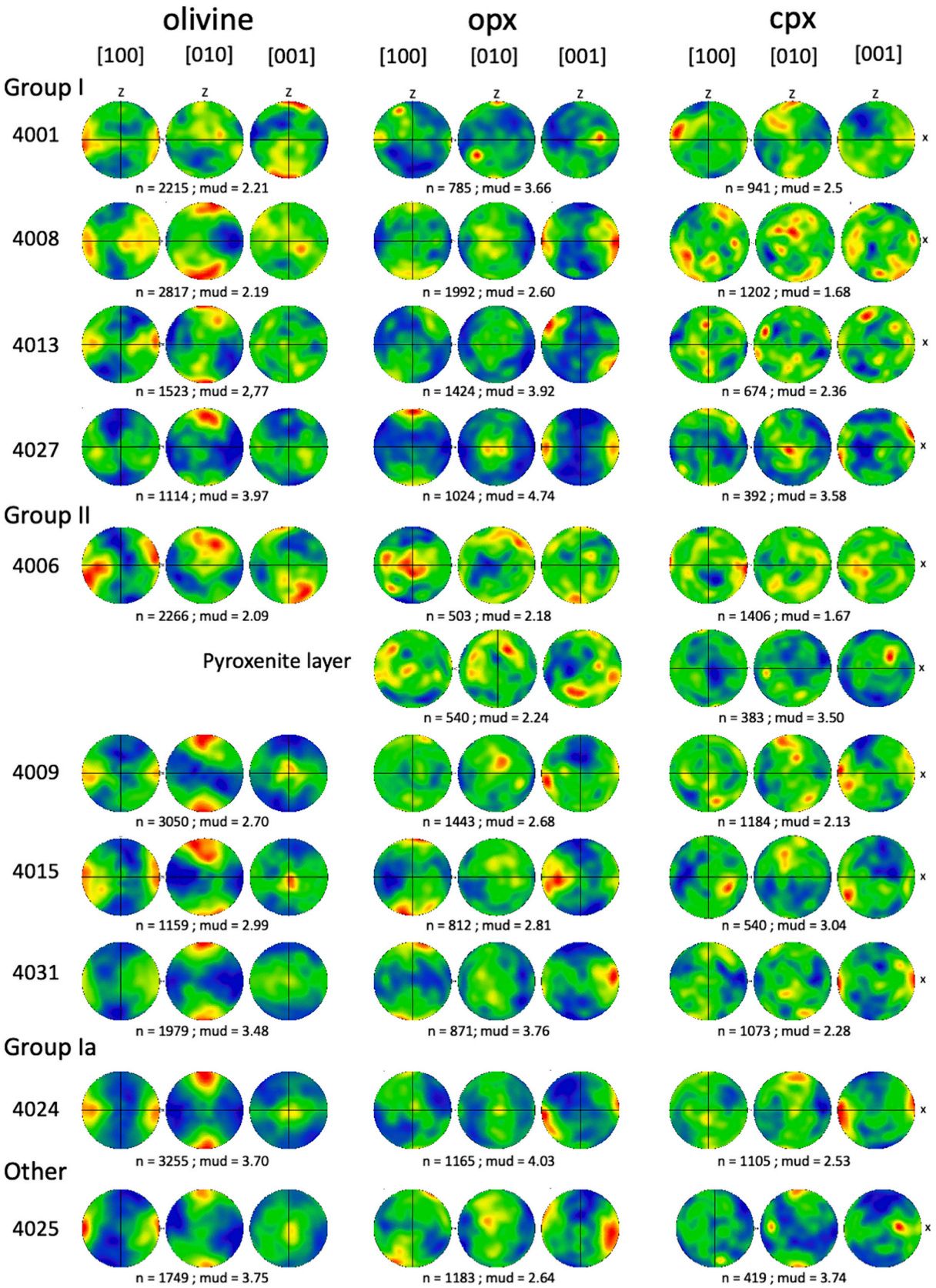

Fig. 5. Pole figures of the crystallographic-preferred orientations (CPO) of olivine, clinopyroxene and micrometric orthopyroxene. The data are displayed as equal-area, stereographic, lower hemisphere projections in the assumed reference frame (X: lineation; Z: normal to foliation), for [100], [010] and [001] axes. Data are represented using average Euler angles for each grain (one point per grain), and coloured as mean uniform density distributions (mud) for contoured plots.

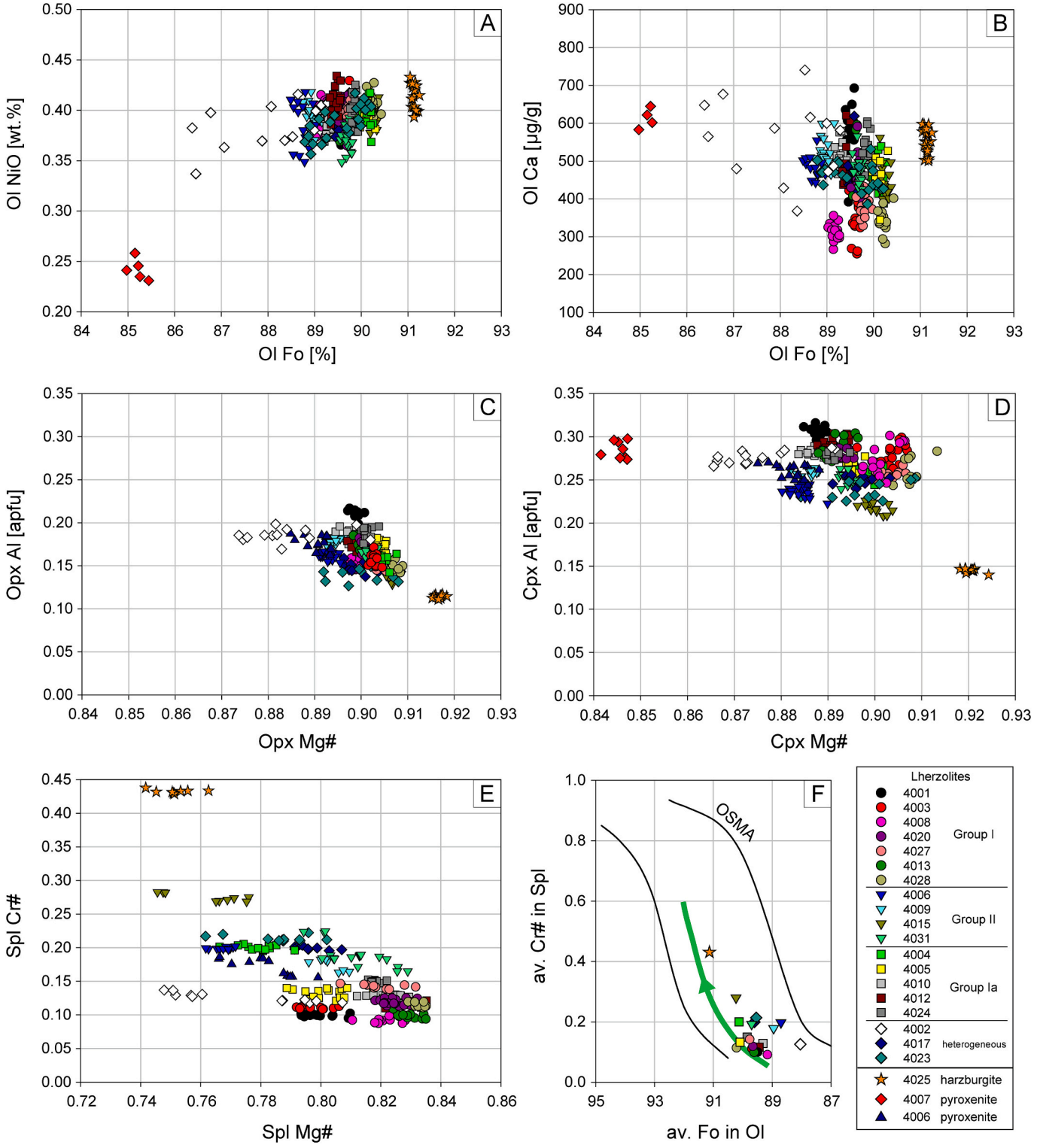

Fig. 6. Major element compositions of primary mineral phases in Mt. Briançon xenoliths (microprobe in-situ analyses). Olivine in Fo-NiO (A) and Fo-Ca diagrams (B); orthopyroxene in Mg#-Al diagram (C); clinopyroxene in Mg#-Al diagram (D); spinel in Mg#-Cr# diagram (E). All individual analyses per sample are displayed. F – spinel Cr# versus olivine Mg# in the olivine-spinel mantle array (OSMA) diagram (Arai, 1994), with a line (green) marking a trend of anhydrous melting at pressures <2 GPa (Scott et al., 2019 and references therein). (For interpretation of the references to colour in this figure legend, the reader is referred to the web version of this article.)

(clinopyroxene). Spinel Cr# is 0.43–0.44. The REE patterns of clinopyroxene are LREE-enriched, but the REE abundances are much lower than those of clinopyroxene from lherzolites (Fig. 7). Orthopyroxene REE patterns are moderately depleted from Lu to Gd and flat from Gd to La with abundances significantly lower than those of orthopyroxene from the lherzolites (Appendix E).

Table 2
Summary of chemical characteristics of xenoliths from Mt. Briançon, averaged data.

cpx REE group	Sample name	Lithology	% Fo	NiO ol [wt%]	Ca ol [μg/g]	Mg# opx	Al opx [apfu]	Mg# cpx	Al cpx [apfu]	Cr# spl
I	4001	lherzolite	89.5	0.39	490–660	0.90	0.211	0.89	0.307	0.10
I	4003	lherzolite	89.6	0.40	260–440	0.90	0.157	0.90	0.280	0.11
I	4008	lherzolite	89.2	0.39	270–360	0.90	0.152	0.90	0.274	0.09
I	4013	lherzolite	89.6	0.39	420–490	0.90	0.173	0.89	0.287	0.10
I	4020	lherzolite	89.7	0.39	400–530	0.90	0.172	0.89	0.280	0.12
I	4027	lherzolite	89.8	0.40	340–460	0.90	0.153	0.90	0.257	0.14
I	4028	lherzolite	90.2	0.40	290–410	0.91	0.147	0.91	0.261	0.11
II	4006	lherzolite	88.7	0.38	440–550	0.89	0.162	0.88	0.237	0.20
II	4009	lherzolite	88.6	0.39	470–580	0.89	0.178	0.89	0.259	0.17
II	4015	lherzolite	90.2	0.40	410–510	0.91	0.139	0.90	0.217	0.28
II	4031	lherzolite	89.7	0.37	430–530	0.90	0.165	0.89	0.251	0.19
Ia	4004	lherzolite	90.1	0.40	390–550	0.90	0.158	0.90	0.258	0.20
Ia	4005	lherzolite	90.1	0.40	450–540	0.90	0.173	0.90	0.268	0.13
Ia	4010	lherzolite	89.3	0.39	470–590	0.90	0.186	0.89	0.282	0.13
Ia	4012	lherzolite	89.5	0.41	440–500	0.90	0.176	0.89	0.291	0.12
Ia	4024	lherzolite	89.9	0.40	470–620	0.90	0.189	0.89	0.279	0.15
variable	4002	lherzolite	88.1	0.39	440–690	0.88	0.186	0.87	0.276	0.13
variable	4017	lherzolite	89.6	0.39	430–530	0.90	0.151	0.90	0.249	0.20
variable	4023	lherzolite	89.5	0.39	390–540	0.90	0.140	0.90	0.237	0.21
other	4025	harzburgite	91.1	0.41	510–670	0.92	0.114	0.92	0.145	0.43
–	4007	olivine clinopyroxenite	85.2	0.24	580–650	–	–	0.85	0.285	–
–	4006	pyroxenite	–	–	–	0.89	0.176	0.88	0.259	0.17

The peridotites are assigned to groups defined by REE contents in clinopyroxene (see Section 4.3 for explanations). Fo – forsterite content in olivine, denoting atomic ratio 100·Mg/(Fetotal + Mg + Mn). Mg# – atomic ratio Mg/(Mg + Fe^{total}). Cr# – atomic ratio Cr/(Cr + Al). Mineral abbreviations: ol (olivine), opx (orthopyroxene), cpx (clinopyroxene), spl (spinel). L-T_{BKN} – temperature calculated with Brey and Köhler (1990) method in spreadsheet from Liang et al. (2013), based on averaged pyroxene compositions. For samples with "no equilibrium"L-T_{BKN} was not calculated due to high variability of major element concentrations in pyroxenes.

4.3.4. Pyroxenites

The pyroxenite layer in composite xenolith 4006 (Fig. 4) contains no olivine. Mg# of ortho- and clinopyroxene are similar or slightly lower than those of pyroxenes in the lherzolitic part (0.88–0.89 and 0.87–0.89, respectively; Fig. 6, Table 2, Appendix A). Orthopyroxene in the pyroxenite layer contains 0.16–0.19 atoms of Al pfu and clinopyroxene contains 0.22–0.25 atoms of Al pfu. Spinel Cr# is 0.16–0.19. REE patterns of ortho- and clinopyroxene are identical to those from the lherzolitic part and thus they are presented together (Fig. 7, Appendix E).

Olivine clinopyroxenite 4007 contains olivine with Fo content of 85.0–85.5%, 0.23–0.26 wt% of NiO and 580–650 μg/g of Ca (Fig. 6, Table 2). Clinopyroxene has Mg# of 0.84–0.85 and contains 0.29 atoms of Al pfu. The REE patterns in clinopyroxene exhibit increasing normalized concentrations from Lu to Nd with Pr–La of similar abundances as Nd (Fig. 7).

4.3.5. Trace elements

Clinopyroxene from Group I lherzolites is characterized by Th and U contents from 5xPM to <0.1xPM, except for lherzolite 4027 where clinopyroxene has Th–U contents between 1xPM and 10xPM (Appendix G). The majority of Group I clinopyroxene exhibits a small positive Sr anomaly. Most of the lherzolites from Groups Ia and II contain clinopyroxene with high concentrations of Th and U (≤10xPM). Group II clinopyroxene exhibits a negative Zr–Hf anomaly. Features common for clinopyroxene in all lherzolites are: concentrations of less incompatible elements (Zr–Lu) from 2xPM to 7xPM, negative Ti and Nb–Ta anomalies of variable depths. A negative Pb anomaly is typical for clinopyroxene in most of the lherzolites.

Harzburgite 4025 contains clinopyroxene that exhibits negative anomalies of Nb(–Ta), Pb, Zr–Hf and Ti (Appendix G). Clinopyroxene from pyroxenite 4007 exhibits well-defined Nb–Ta, Pb, Sr and Ti negative anomalies and slight Zr–Hf negative anomaly (Appendix G).

Trace element abundances in orthopyroxene from all peridotites are slightly lower than those of PM for the most compatible elements, decreasing to ~0.1xPM for less compatible elements. Typically, positive anomalies of U (rarely with Th), Zr–Hf and Ti occur. In contrast to the lherzolites, orthopyroxene from harzburgite 4025 exhibits only slight positive Ti anomaly and no Zr–Hf anomaly (Appendix E).

4.4. Geothermometry

Temperatures calculated on a basis of major element analyses in pyroxene pairs (T_{BKN}; Brey and Köhler, 1990) define two groups of peridotites. The majority of samples yielded results that are consistent between pyroxene cores and rims at the scale of the thick section, with differences between minimal and maximal T_{BKN} of 19–40 °C. T_{BKN} ranges from 991 to 1081 °C (Table 3). Temperatures based on REE contents in pyroxenes (T_{REE}; Liang et al., 2013) yielded results from 1009 ± 4 °C to 1113 ± 5 °C (Table 3). The samples belonging to this group are: 4001, 4020 (Group I with LREE-depleted clinopyroxene), 4009, 4015, 4031 (Group II with LREE-enriched clinopyroxene), all peridotites from Group Ia (spoon-like REE patterns in clinopyroxene), lherzolite 4002 (heterogeneous clinopyroxene REE contents) and harzburgite 4025. All of them exhibit porphyroclastic texture and contain high-Ca olivine and orthopyroxene, except lherzolite 4020 with high-Ca rims and low-Ca cores in orthopyroxene.

Seven samples constitute the second group, exhibiting differences in T_{BKN} of 40–80 °C between cores and rims in single grains. The T_{BKN} in the cores are typically lower (839–996 °C) than those in the rims (920–1054 °C). Within a sample, temperatures can also vary, with the lowest and the highest result differing typically by 16 to 37 °C (ΔT_{BKN}) for cores and 18–40 °C for rims. Clinopyroxene cores in some samples yield greater ΔT_{BKN}: 94 °C (lherzolite 4008), 47 °C (lherzolite 4028), 52 °C (lherzolite 4006) and 54 °C (lherzolite 4017). This group comprises the majority of peridotites form Group I (LREE-depleted clinopyroxene), lherzolite 4006 (Group II) and lherzolites 4023 and 4017 with heterogeneous clinopyroxene REE contents. Most of those samples contain low-Ca olivine and orthopyroxene, with only lherzolites 4013 and 4023 containing high-Ca olivine and orthopyroxene.

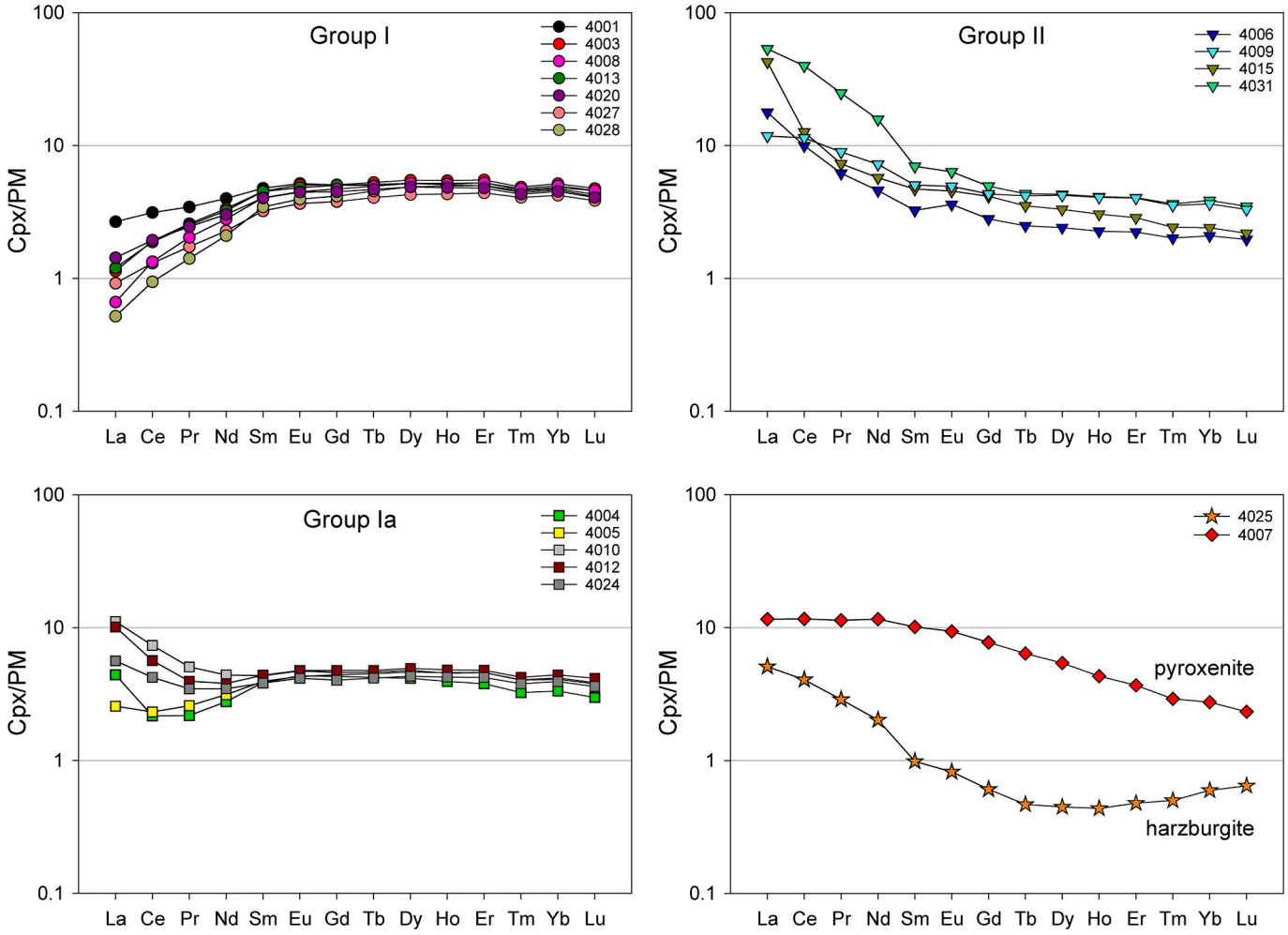

Fig. 7. REE patterns of clinopyroxene from Mt. Briançon xenoliths showing averages of multiple in-situ LA-ICP-MS analyses for the different groups and lithologies identified in this study. The data are normalized to primitive mantle (PM, values after McDonough and Sun, 1995).

5. Discussion

5.1. Origin of clinopyroxene: general considerations based on evidence from EBSD

The Mt. Briançon xenoliths represent the southern mantle domain of the Massif Central (Fig. 1). The occurrence of lherzolites with LREE-depleted clinopyroxene is the most typical feature of this domain (e.g. Downes et al., 2003; Puziewicz et al., 2020). Two contrasting interpretations of these characteristics have been proposed. Some authors indicate that depletion in LREE is a result of low-degree partial melting (e.g., Touron et al., 2008; Uenver-Thiele et al., 2017). The second interpretation, suggested by Lenoir et al. (2000) and supported by Downes et al. (2003), is that this kind of clinopyroxene was formed by metasomatism with melts of MORB affinity. The recent study of Puziewicz et al. (2020) supports the second interpretation, showing by means of fabric study that LREE-depleted clinopyroxene is a later addition to the pre-existing olivine-orthopyroxene framework of the lherzolites.

The xenolith suite described in this paper consists almost entirely of lherzolites (Fig. 3). However, three different groups of these rocks are defined based on the clinopyroxene REE compositions (Fig. 7): (1) lherzolites with LREE-depleted clinopyroxene (Group I), (2) lherzolites with clinopyroxene of spoon-like REE patterns (Group Ia) and (3) lherzolites containing LREE-enriched clinopyroxene (Group II).

Crystallographic preferred orientation (CPO) study reveals two basic types of relationships between the mineral phases in the lherzolites (Fig. 5): (a) orthopyroxene [001] axes are parallel or sub-parallel to olivine [100] axes and to the lineation (X), both defining the fabric of the rock, whereas clinopyroxene exhibits scattered CPO with crystallographic orientations discordant to olivine-orthopyroxene framework, and (b) orthopyroxene and clinopyroxene [001] axes are parallel or sub-parallel to olivine [100] axes, all defining the fabric of the rock. The REE composition of clinopyroxene and the CPO of minerals are correlated. Group I lherzolites display clinopyroxene CPO discordant to the olivine-orthopyroxene fabric (Figs. 5 and 7). In contrast, clinopyroxene in lherzolites from Group Ia and Group II exhibits CPO that is consistent with those of olivine and orthopyroxene.

Our interpretation is that if clinopyroxene does not fit the fabric defined by olivine and orthopyroxene, then it is a metasomatic phase which was formed or modified under suprasolidus conditions by pervasive melt percolation. The melt percolating interstitially in a peridotite host can add new clinopyroxene or can react with the existing one and modify its composition as well as its crystallographic orientation in case of complete replacement (e.g. Jean et al., 2010; Kaczmarek et al., 2015; Rospabé et al., 2017). For melt to percolate, the host peridotite must contain an interstitial melt network, which in turn requires suprasolidus conditions (Puziewicz et al., 2023). Reactive melt percolation is able to modify large volumes of rock, at the scale of kilometres (e.g. Le Roux et al., 2007; Van der Wal and Bodinier, 1996, and references therein). Phase relationships in a suprasolidus region of the lherzolite (e.g. Jennings and Holland, 2015) indicate that in Group I also spinel was added or modified by the metasomatic agent. Indeed, co-

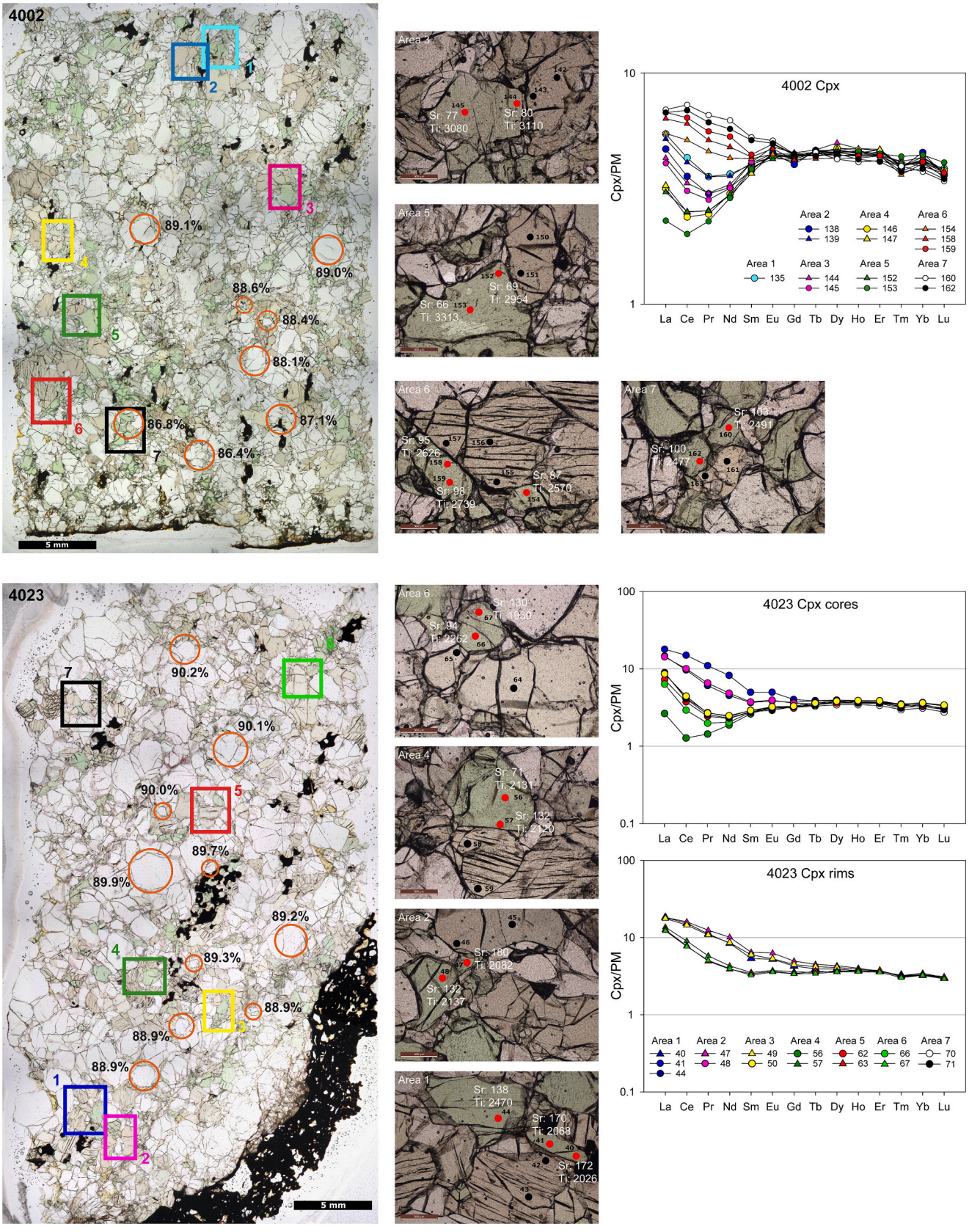

Fig. 8. Chemical composition of olivine and clinopyroxene grains in lherzolites 4002 and 4023, displaying variation relative to the location of minerals. Circles mark location of analysed olivine grains and numbers in percent denote Fo content in olivine cores. Fo contents in the rims are equal to or up to 0.2% higher/lower than those in cores. Rectangles mark areas of clinopyroxene REE analyses. Individual analyses of cores and rims are shown in the PM-normalized REE diagrams. Analyses of core and rim in the same grain have the same colour. The microphotographs of the areas show ablation spots localizations and Sr and Ti contents of respective analyses in ppm. Note that microphotographs of the areas are rotated by 90° relative to orientation of whole-section images.

Table 3
Results of geothermometric calculations for Mt. Briançon peridotites.

Sample name	REE cpx group	Lithology	T_{BKN} min-max °C (n)	average cores $T_{BKN} \pm 1\sigma$ °C	average rims $T_{BKN} \pm 1\sigma$ °C	L-T_{BKN} °C	$T_{REE} \pm 1\sigma$ °C	average T °C
4001	I	lherzolite	1042–1076 (6)	1060 ± 11	1051 ± 11	1059	1073 ± 5	1063
4003	I	lherzolite	919–935 (6) *967–986 (6)	935 ± 13	954 ± 21	–	–	–
4008	I	lherzolite	839–933 (5) *920–956 (5)	889 ± 33	937 ± 12	–	–	–
4013	I	lherzolite	974–996 (5) *1019–1037 (5)	988 ± 9	1029 ± 7	–	–	–
4020	I	lherzolite	1003–1039 (6)	1023 ± 15	1027 ± 6	1031	1063 ± 9	–
4027	I	lherzolite	966–993 (6) *974–1014 (6)	976 ± 11	996 ± 15	–	–	–
4028	I	lherzolite	910–957 (5) *933–966 (5)	927 ± 21	946 ± 12	–	–	–
4006	II	lherzolite	972–1024 (8) *960–1025 (8)	996 ± 19	1001 ± 21	–	–	–
4009	II	lherzolite	1044–1063 (6)	1059 ± 3	1048 ± 4	1055	1104 ± 5	–
4015	II	lherzolite	998–1030 (6)	1016 ± 13	1014 ± 10	1017	1041 ± 6	1024
4031	II	lherzolite	1021–1044 (6)	1034 ± 10	1031 ± 2	1035	1060 ± 7	1035
4004	Ia	lherzolite	1005–1042 (5)	1014 ± 8	1027 ± 10	1021	1009 ± 4	1018
4005	Ia	lherzolite	991–1029 (6)	1008 ± 12	1003 ± 11	1007	1034 ± 6	1014
4010	Ia	lherzolite	1041–1081 (4)	1070 ± 10	1053 ± 8	1063	1099 ± 8	–
4012	Ia	lherzolite	1012–1048 (7)	1026 ± 14	1039 ± 6	1033	1022 ± 6	1029
4024	Ia	lherzolite	1043–1069 (6)	1057 ± 8	1041 ± 8	1051	1100 ± 6	–
4002	variable	lherzolite	1021–1055 (7)	1038 ± 11	1029 ± 6	1036	1064 ± 6	1044
4017	variable	lherzolite	978–1048 (6) *1013–1048 (6)	1005 ± 21	1032 ± 12	–	–	–
4023	variable	lherzolite	958–995 (5) *1018–1054 (5)	970 ± 11	1024 ± 6	–	–	–
4025	other	harzburgite	1028–1074 (5)	1055 ± 14	1037 ± 11	1048	1113 ± 5	–

The samples are arranged in the same order as in Table 2. T_{BKN} – minimal and maximal temperature in the sample calculated using Brey and Köhler (1990) method; n – number of pyroxene pairs used. Samples with two T_{BKN} ranges yielded significant differences in temperatures between cores and rims at the scale of grains, upper range is for cores, lower one (marked with *) is for rims. L-T_{BKN} – temperature calculated with Brey and Köhler (1990) method in spreadsheet from Liang et al. (2013), based on averaged pyroxene compositions. T_{REE} – temperature calculated using method of Liang et al. (2013). Average T – a temperature calculated as average of T_{BKN}, L-T_{BKN} and T_{REE} (see Section 3.5 for explanations) for samples where differences between those temperatures were no >40 °C.

precipitation of clinopyroxene and spinel from metasomatic melt has been noted in CLM samples before (e.g. Lorand et al., 2013; Wittig et al., 2010).

In the second type of relationship, olivine, orthopyroxene and clinopyroxene exhibit consistent CPO (Fig. 5). This indicates that they all were concomitantly deformed and that their fabric has not been modified subsequently.

All lherzolites and harzburgite studied by EBSD display olivine fabrics which suggests the activation of the A-type [100](010) slip system (Katayama et al., 2004). This slip system is the most common in the upper mantle and is well studied in the continental lithospheric mantle (e.g. Hidas et al., 2019; Kaczmarek et al., 2016; Tommasi et al., 2000; Tommasi and Vauchez, 2015) and is activated at low strain and high-temperature deformation (Ben Ismaïl and Mainprice, 1998; Nicolas et al., 1971). The exception is lherzolite 4001, containing olivine of *E*-type slip system, which is also common in nature (e.g. Mehl et al., 2003; Michibayashi and Mainprice, 2004; Sawaguchi, 2004; Skemer et al., 2010) and could represent similar conditions with small addition of water in the olivine (Katayama et al., 2004) and also high melt contents under high temperatures (Tommasi et al., 2006).

5.2. Petrogenesis of Group I lherzolites

5.2.1. Mineral crystallization sequence

Lherzolites of Group I contain 51–65 vol% of olivine and 10–16 vol% of clinopyroxene (Fig. 3, Table 1). An exception is lherzolite 4027 containing 75 vol% of olivine and 5 vol% of clinopyroxene. The Group I lherzolites do not plot on the melting paths of lherzolite to harzburgite on the ultramafic ternary diagram (Fig. 3). This group contains orthopyroxene with [001] parallel or sub-parallel to olivine [100] axes (Fig. 5). Both minerals are weakly deformed. Clinopyroxene has scattered crystallographic orientation, and its axes are discordant relative to olivine-orthopyroxene framework (Fig. 5). Consequently, the clinopyroxene in Group I lherzolites is interpreted as a metasomatic phase.

Lherzolite 4013 contains orthopyroxene with point concentrations on [001] axes that are at 45° to olivine [100], suggesting that those phases were not deformed together (Fig. 5). Clinopyroxene from this sample exhibits scattered orientation with no strong crystallographic relations with orthopyroxene CPO. A few clinopyroxene grains display [001] axes at low angle to orthopyroxene [001] axes (Fig. 5). This crystallographic orientation of orthopyroxene discordant to olivine may be a record of conditions under which orthopyroxene could have crystallized and/or recrystallized during melt percolation.

Group I lherzolites contain some of the most aluminous and the least chromian spinel in the studied peridotite suite, with Cr# of 0.09–0.12 (Fig. 6, Table 2). Clinopyroxene contains 0.25–0.32 atoms of Al pfu, with that from lherzolite 4001 exhibiting the highest values (0.30–0.32 apfu) and that from 4027, 4028 the lowest ones (~0.25–28 apfu). In the case of a secondary origin of clinopyroxene, this variability may result from evolution of the metasomatic melt that reacted with the rock, whereas in case of overprint, it may result or be strengthened by variable chemical compositions of the protolith. Orthopyroxene Al content (Fig. 6, Table 2, Appendix A) is the lowest in lherzolites 4003, 4008, 4027, 4028 (0.14–0.17 apfu) and highest in lherzolite 4001 (0.20–0.22 apfu). Because a primary origin for this mineral is suggested, chemical variability of the protolith could have been an important factor affecting Al content.

5.2.2. Metasomatic agent and process

Assuming no additional (later) metasomatic modifications of Group

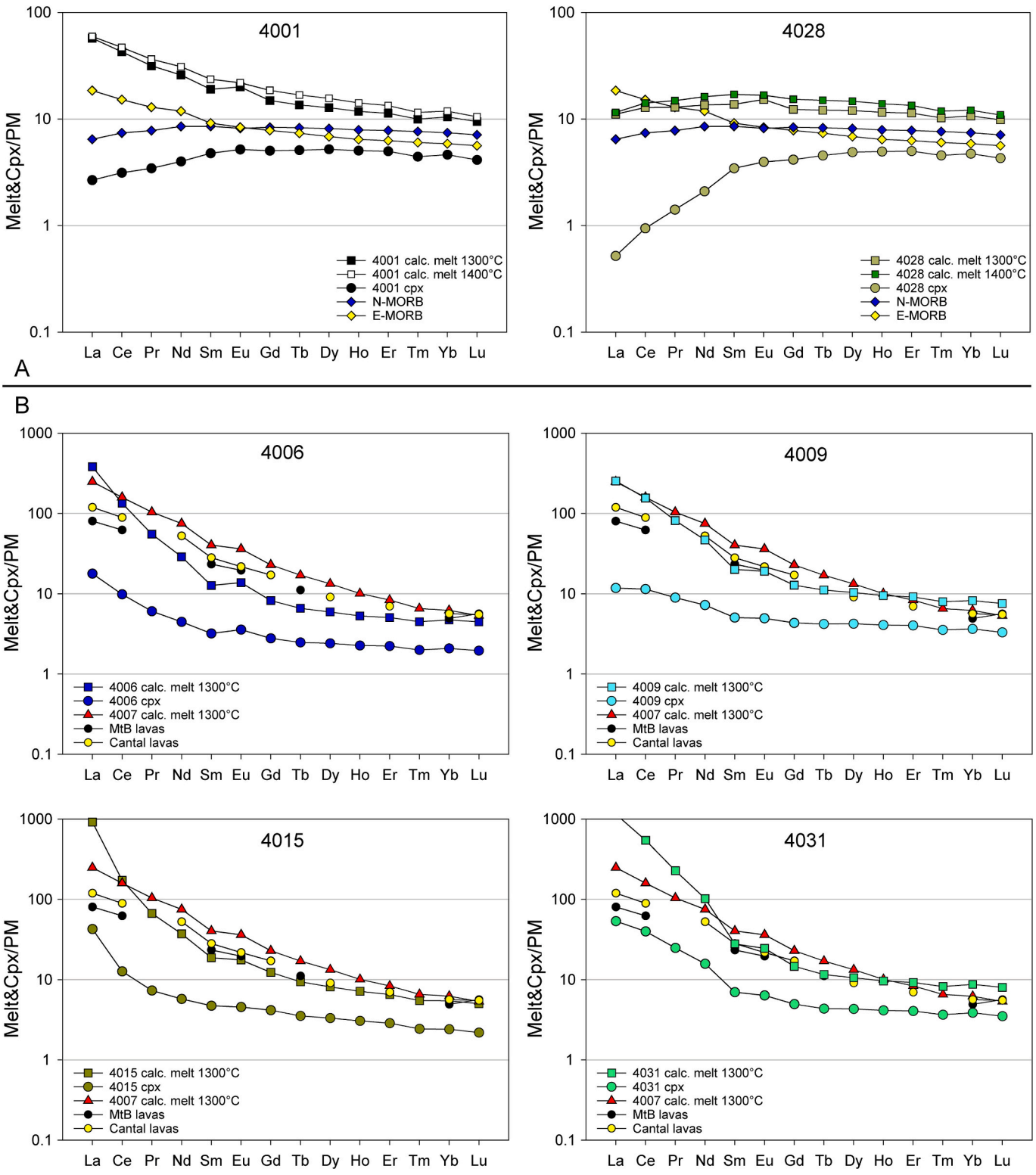

Fig. 9. A – REE compositions of clinopyroxene from Group I lherzolites (circles) and calculated hypothetical melt in equilibrium with this clinopyroxene (squares) compared with typical N-MORB and *E*-MORB REE compositions (diamonds). Data for MORB from: Gale et al. (2013). B – REE compositions of clinopyroxene from Group II lherzolites (circles) and calculated melts in equilibrium with this clinopyroxene (squares) compared with clinopyroxene from pyroxenite 4007 (red triangles), Mt. Briançon lavas (black circles, data from: Liotard et al., 1988) and Cantal lavas (green circles, sample MC1 from: Chauvel and Jahn, 1984). See text for information on distribution coefficients used in the calculations. (For interpretation of the references to colour in this figure legend, the reader is referred to the web version of this article.)

I, we calculated hypothetical melts in equilibrium with clinopyroxene from two Group I lherzolites (Fig. 9A), bearing in mind that the samples are now subsolidus, and that some elements may therefore be affected by subsolidus re-equilibration, such as HFSE (e.g., Rampone et al., 1991; Witt-Eickschen and O'Neill, 2005) and REE (Sun and Liang, 2014). For this, we used clinopyroxene REE compositions and partition coefficients between clinopyroxene and melt applicable to melting of DMM (depleted MORB mantle) at 1300 °C and 1400 °C (Yao et al., 2012). Two chosen lherzolites were: (1) 4001 with clinopyroxene that is the least depleted in LREE and (2) 4028 with clinopyroxene that is one of the most depleted in LREE. The calculated melts (Fig. 9A) have REE compositions similar to those typical for E-MORB and N-MORB, respectively (Gale et al., 2013). The differences in REE concentrations between calculated melt and MORB occur possibly due to the fact that Yao et al. (2012) obtained the partition coefficients from experiments in suprasolidus conditions, whereas our rocks reached their final equilibrium in subsolidus conditions. This could have led to redistribution of REE between coexisting ortho- and clinopyroxene, increasing their concentrations in clinopyroxene (e.g. Sun and Liang, 2014). Even so, the MORB-affinity of LREE-depleted clinopyroxene from lherzolites from Mt. Briançon and other localities in the southern domain of the Massif Central is confirmed by Sr and Nd isotopic study of Downes and Dupuy (1987) who report $^{87}Sr/^{86}Sr$ of 0.70234–0.70284 (εSr from −30.7 to −23.6) and $^{143}Nd/^{144}Nd$ of 0.513130–0.513354 (εNd from +9.4 to +13.9). Downes and Dupuy (1987) indicate that this kind of clinopyroxene composition is typical for a depleted MORB-source mantle. Our data are another example of the generation of MORB-like melts in a subcontinental lithospheric mantle context (Puziewicz et al., 2023).

5.3. Petrogenesis of Group II lherzolites

5.3.1. Mineral crystallization sequence

Lherzolites of Group II contain 67–83 vol% of olivine and 5–9 vol% of clinopyroxene (Fig. 3, Table 1), which makes them the richest in olivine and the poorest in clinopyroxene among the studied rocks (Fig. 3). They consist of olivine and orthopyroxene that were deformed together. In these lherzolites, clinopyroxene [001] axes are parallel or sub-parallel to olivine [100] axes and to orthopyroxene [001] axes (Fig. 5). Thus, the clinopyroxene CPO is coherent with the fabric defined by olivine and orthopyroxene, suggesting that olivine and pyroxenes were deformed together.

Spinel in Group II lherzolites is more chromian than that from Group I (Fig. 6, Table 2). Typical Cr# is 0.16–0.22 and in lherzolite 4015 it is 0.27–0.28. Clinopyroxene is the least aluminous among all the lherzolites (0.21–0.26 atoms of Al pfu), with that from lherzolite 4015 having the lowest Al content (0.21–0.22 apfu). Average Ti concentrations in clinopyroxene from Group II are 1805–2644 μg/g and average Sr concentrations (117–327 μg/g) are more variable, compared to 2992–4030 μg/g and 52–88 μg/g, respectively in Group I lherzolites (Appendix B). This makes Group II clinopyroxene the poorest in Ti and the richest in Sr among all the lherzolites.

Lherzolite 4031 contains clinopyroxene that is more enriched in LREE than that from the rest of Group II (Fig. 7). Additionally, its orthopyroxene is significantly less depleted in LREE than orthopyroxene in any other studied sample (Appendix E). The shapes of REE patterns in both clino- and orthopyroxene are almost identical to those from harzburgite 4025. However, those two rocks differ in pyroxene REE and other trace elements concentrations. Additionally, lherzolite 4031 clinopyroxene exhibits a strong Nb–Ta anomaly (Appendix G), whereas the anomaly is only slight in harzburgite 4025.

5.3.2. Metasomatic agent and clinopyroxenite genesis

We calculated hypothetical melts in equilibrium with clinopyroxene from Group II lherzolites, using their REE compositions and partition coefficients given by Yao et al. (2012). The resulting melt compositions are similar to those typical of alkaline basaltic melts (Fig. 9B). We compared the calculated melts to available REE data on Mt. Briançon Cenozoic alkaline lavas (Liotard et al., 1988) and similar Cantal lavas (Chauvel and Jahn, 1984). The REE patterns of calculated melts for lherzolites 4006, 4009 and 4015 are generally parallel to those lavas but have slightly elevated concentrations of La, Ce and Pr. Sample 4006 is a composite xenolith (Fig. 4A) with orthopyroxene [100] axes from the pyroxenite similar to CPO of lherzolitic orthopyroxene, and the degree of internal deformation of orthopyroxene in the pyroxenitic layer similar to the degree of deformation recorded by olivine. This suggests a common deformation history of both parts of the sample. Also, the trace element concentrations of ortho- and clinopyroxene from the lherzolite are identical to those of pyroxenes from the pyroxenite layer. Pyroxenes from both the lherzolite and the pyroxenite part of the sample are similar to alkaline lavas of the Massif Central. Therefore, we suggest that the majority of Group II lherzolites contain pyroxenes that were modified by alkaline melts that are similar but not identical to compositions of the Cenozoic volcanics of the Massif Central. In contrast, calculated melt in equilibrium with clinopyroxene in olivine clinopyroxenite 4007 (Fig. 4B) is almost identical to the Massif Central lavas (Fig. 9B). It is therefore possible that this pyroxenite represents veins of crystallized melt introduced into the lithosphere by Cenozoic volcanic activity.

For clinopyroxene from 4031, the calculated melt is less similar to the Mt. Briançon Cenozoic lavas for clinopyroxene from 4031, exhibiting higher La–Nd contents (Fig. 9B). Taking into account the differences between lherzolite 4031 and the rest of Group II described in Section 5.4.1, it is possible that this rock records a different metasomatic event than other Group II lherzolites, or that the metasomatic agent was more fractionated, e.g., due to earlier reactive melt percolation (e.g. Tilhac et al., 2021; Vernières et al., 1997).

5.3.3. Nature of metasomatism

The relationships in lherzolite 4023 (see 5.3) suggests that the volcanism that formed the Devès volcanic field is responsible for the overprint of Group II lherzolites, and that at least part of those lherzolites acquired their LREE-enriched characteristics after source rock fragmentation and entrainment in the erupting melt. However, lherzolites forming Group II are petrographically similar to each other (relatively high olivine and low clinopyroxene contents, spinel of high Cr#) and distinct from those of Group I. This suggests that they come from mantle region which was not subjected to the extensive melt percolation that formed Group I lherzolites. The protolith of Group II was supposedly more sensitive to *syn*-volcanic metasomatism compared to lherzolites of Group I. This may be due to its greater refractoriness, accompanied by a small content of clinopyroxene, whereas the clinopyroxene-rich Group I lherzolites were buffered against overprint by a small-volume melt by their fertile compositions. Thus, Group II lherzolites formed in mantle lithologies which escaped MORB-like metasomatism that produced LREE-depleted lherzolites of Group I.

In summary, the LREE-enriched characteristic of Group II is a result of alkaline melt metasomatism related to Cenozoic volcanism. The homogeneous major and trace element distribution in clinopyroxene shows that the metasomatism operated long enough to overprint pre-existing chemical characteristic of this mineral, which is here interpreted as residual in origin.

5.3.4. Lherzolite 4027 – transitional between Group I and Group II?

Lherzolite 4027 contains clinopyroxene with [001] axes that are at slight angle (<45°) to orthopyroxene [001] axes, therefore CPO correlation is similar to that of rocks of Groups II (olivine [100] are parallel to orthopyroxene and clinopyroxene [001] axes) (Fig. 5). This similarity is manifested also by significantly higher olivine and lower clinopyroxene contents relative to other lherzolites of Group I (Fig. 3, Table 1) as well as relatively high Cr# of spinel (0.14; Fig. 6, Table 2). Nevertheless, the clinopyroxene is characterized by REE and trace element contents typical for Group I lherzolites (Fig. 7). These relationships suggest that Group I lherzolites could have originated by MORB-metasomatism (see

above) of an olivine-rich protolith (possibly corresponding to Group II lherzolites) which added clinopyroxene at the cost of olivine. If so, lherzolite 4027 may record an early stage of metasomatism by MORB-like melt when a relatively small volume of melt has percolated through the rock, which affected its chemical characteristics, but did not change the primary CPO of clinopyroxene. In contrast, most of the Group I lherzolites are suggested to have originated due to percolation of larger time-integrated volumes of MORB-like melt through the protolith, which enabled formation of larger volumes of clinopyroxene at the cost of olivine and significantly affected the fabric.

5.4. Petrogenesis of Group Ia lherzolites

Lherzolites from Group Ia have the most variable modal compositions, with the majority containing less olivine (46–66 vol%) and more clinopyroxene (11–26 vol%) than those from Group II (Fig. 3, Table 1). In lherzolite 4024 from Group Ia, olivine (66 vol%), ortho- and clinopyroxene have CPO similar to those in Group II (Fig. 5). Olivine has [100] axes parallel to X, and orthopyroxene and clinopyroxene [001] axes are parallel to olivine [100] axes, indicating concordant deformation of all three phases (Fig. 5) but it would be too speculative to make generalized interpretations based on CPO data from one sample.

The content of Al in clinopyroxene from Group Ia is similar to that of clinopyroxene from Group I. Group Ia clinopyroxene contains 2804–3430 μg/g of Ti and 59–115 μg/g of Sr, similarly to clinopyroxene from Group I (Appendix B). The majority of Group Ia lherzolites contain spinel with Cr# 0.11–0.15 which is close to that from Group I lherzolites (Fig. 6, Table 2). Lherzolite 4004 from Group Ia contains spinel with Cr# 0.20, resembling that from Group II. In general, lherzolites of Group Ia are transitional between Groups I and II in terms of REE compositions of pyroxenes (Fig. 7). Regarding geochemical evidence, the suggested relationship between lherzolites of Group I and II indicates that those of Group Ia could represent Group I that was modified by relatively small volumes of percolating alkaline melt, but, having much more clinopyroxene, it was less affected, acquiring spoon-like REE patterns rather than highly LREE-enriched ones.

5.5. Chemical and thermal evolution of the refertilized CLM beneath Mt. Briançon

Three lherzolites from the studied suite (4002, 4017, 4023) contain silicates with variable Mg# across the thick section and clinopyroxene with varying LREE contents (Fig. 8, Appendix F). *Lherzolite 4017* exhibits no systematic variation of chemical parameters across the section (Appendix F), which may be due to unfavourable sectioning, and it is not further considered here. In contrast, *lherzolite 4002* (Fig. 8) comprises two areas, of which one consists of olivine with Fo 89, coexisting with clinopyroxene with LREE-depleted spoon-like patterns, 70–80 μg/g of Sr and ~ 2900 μg/g of Ti. Another area contains olivine with Fo 86–87 coexisting with LREE-enriched clinopyroxene with ~100 μg/g of Sr and ~ 2400 μg/g of Ti (Fig. 8). Spinel (Cr# 0.13) is compositionally homogeneous at the scale of the section. The first area is similar to Group Ia lherzolites, whereas the second one corresponds to Group II (Fig. 7). Clinopyroxene of Group Ia contains ~60–120 μg/g Sr and 2700–4000 μg/g Ti, whereas that of Group II contains 110–370 μg/g Sr and 1500–3000 μg/g Ti. This section is interpreted to show the contact between lherzolites of Groups Ia and II.

Lherzolite 4023 exhibits foliation, defined by elongation of spinel aggregates and elongation of olivine aggregates. The LREE content in clinopyroxene varies not only across the section but also between cores and rims of single grains (Fig. 8). Three grains, occurring near the contact with the host basanite, are completely LREE-enriched (areas 1 and 2 in Fig. 8). The surrounding olivine has ~Fo89. The clinopyroxene grain occurring in area 3, located also close to the contact, is similar to the rest of analysed grains (areas 3–6), which have LREE-enriched rims and cores with spoon-shaped patterns. Cores of clinopyroxene grains contain 70–100 μg/g of Sr, whereas rims contain 130–175 μg/g, except a small interstitial grain from area 7 (Fig. 8) which contains 115 μg/g of homogeneously distributed Sr. These grains coexist with olivine having Fo90. The Ti content (~1900–2500 μg/g) shows no systematic variation at the scale of grains. Spinel has Cr# of 0.20, which is high compared to the most of lherzolites (Fig. 6, Table 2). The core-rim relationships suggest that the protolithic lherzolite contained clinopyroxene with spoon-shaped LREE patterns (similar to Group Ia), the rims of which were modified to LREE-enriched ones. Because this modification affected entire grains close to the contact with the host scoria, but affected only rims further inside the xenolith (Fig. 8), the process likely operated while the xenolith was entrained in the host basanite scoria. Similar entrainment effects were described by Marchev et al. (2017) in xenoliths occurring in basanite domes in northern Bulgaria.

We used the REE contents in margins and centres of REE-zoned grains in lherzolite 4023 to calculate temperatures using the Liang et al. (2013) thermometer (Appendix C). The results show systematic differences between core and rim in the majority of calculated single-grain temperatures, with rims yielding temperatures higher by 48–112 °C than cores. In the thermally equilibrated samples from a xenolith suite from Befang in the Cameroon Volcanic Line, the variation in temperatures calculated for individual points in single grains is <20 °C (Tedonkenfack et al., 2021), which is true for only two out of six analysed grains in lherzolite 4023 (Appendix C).

The majority of Group I lherzolites exhibits variability of calculated T_{BKN} temperatures at the pyroxene grain scale, with rims yielding temperatures higher than cores by 40–80 °C (Table 3). This suggests that those rocks were affected by a thermal pulse that modified composition of pyroxene rims but was not long-lasting enough to affect grain cores. We suggest that this was related to an incipient alkaline metasomatic event, recorded in lherzolite 4023, and that it is a result of Cenozoic volcanic activity in the Massif Central.

5.6. Petrogenesis of harzburgite

Harzburgite 4025 consists of an olivine-orthopyroxene framework in which almost undeformed clinopyroxene occurs (Fig. 5). This kind of texture is identical to that characterizing the lherzolites of Group I. The harzburgite contains 73 vol% of olivine and 3.5 vol% of clinopyroxene. (Fig. 3, Table 1). The olivine content is similar to those from Group II lherzolites (67–83 vol% of olivine), which are also the poorest in clinopyroxene (5–9 vol%) among the lherzolites.

Harzburgite 4025 consists of silicate minerals that have significantly higher Mg and Ca contents and lower Al, Fe, Ti and Na contents than silicates from the lherzolites (Fig. 6, Appendix A). It also contains highly chromian spinel (Cr# 0.43). The major element composition of minerals resembles those of LREE-enriched harzburgites from the Allègre and Alleyras localities (Puziewicz et al., 2020) as well as those of harzburgites from the northern domain of the Massif Central (Uenver-Thiele et al., 2017 and references therein). In contrast, REE and other trace element concentrations in clinopyroxene from harzburgite 4025 (Fig. 7, Appendix G) are significantly lower than those from Allègre and Alleyras harzburgites. The REE pattern of harzburgite 4025 clinopyroxene is similar to that from one sample (Z42b) from the Zanières locality, reported by Downes et al. (2003). These authors suggest that because Zanières is located close to the boundary between domains determined by Lenoir et al. (2000), xenoliths found there may exhibit characteristics that are transitional between the northern and southern domain. Although Mt. Briançon is located further into the southern domain, the boundary between the domains is not well resolved in the eastern part of Massif Central due to scarce xenolith occurrences in the Limagne Graben region. It is also possible that harzburgite 4025 represents a small fragment of "northern-type mantle" embedded into southern domain or that it comes from a different lithospheric mantle level compared to the lherzolites.

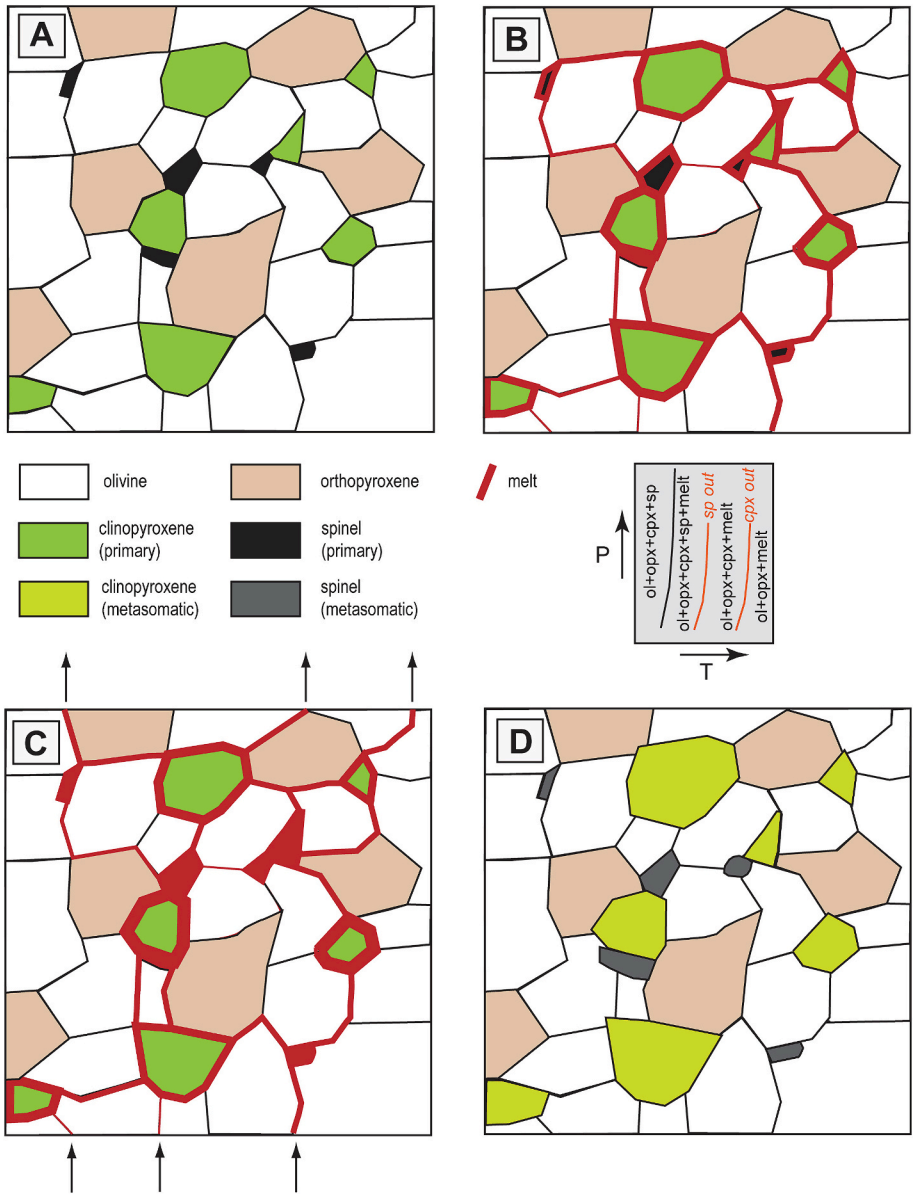

Fig. 10. Simplified model of the origin of Group I lherzolites. The model follows the details presented in Puziewicz et al. (2023), phase relationships are from the Jennings and Holland (2015) model of lherzolite KLB-1 melting. The "clinopyroxene out" corresponds to ~20% of generated melt at 1.5 GPa (see inset below panel B). The protolith (Ol 68 vol%, Opx 21 vol%, Cpx 9 vol%, Spl 2 vol%) has a composition similar to that of lherzolite 4009 described in this study and is richer in olivine relative to KLB-1 (Ol 58 vol%, Opx 26 vol%, Cpx 14 vol%, Spl 2 vol%; Davis et al., 2009).
The protolith (A) starts to melt and a film of melt in equilibrium with the host rock is formed (B). This enables the percolation of external melt, which is not in equilibrium with the host and reacts with it (C). The volume of melt is ≤12 vol%, but the time-integrated melt volume may be much greater if the percolation is prolonged. The reaction is peritectic and below the "clinopyroxene out" curve (see inset) consumes mostly spinel and clinopyroxene, subordinately orthopyroxene (see eg. Gudfinnsson and Presnall, 2000). The composition and volume of all minerals changes gradually. Olivine and large part of the orthopyroxene preserve their primary crystallographic orientation, whereas clinopyroxene and spinel are virtually all replaced, and, if accompanied by newly-formed minerals, their volume can be different from that in the protolith (D). All melts generated or consumed by peritectic reaction(s) have basaltic compositions.

6. Conclusions

The Mt. Briançon xenolith suite comprises three different groups of lherzolites, designated in this study as Group I, Group Ia and Group II. The combined mineral chemical and textural data indicate that the lherzolites of Group I originated by MORB-like melt metasomatism of a peridotitic protolith, in which primary clinopyroxene and possibly spinel were replaced or in part added at suprasolidus conditions (Fig. 10). The xenoliths of Group I lherzolites, containing LREE-depleted clinopyroxene, are common in the Mt. Briançon xenolith suite, suggesting that this kind of rock is volumetrically significant in the lithospheric mantle if not preferentially sampled by the host magma.

Group II lherzolites constitute a subordinate lithology that is significantly enriched in olivine and impoverished in clinopyroxene compared to Group I lherzolites, and contains spinel of higher Cr#. These rocks, which escaped MORB-like metasomatism, are LREE-enriched, which is commonly attributed to a "metasomatic reaction front" preceding the massive melt metasomatism, documented in orogenic peridotite massifs like e.g. Lherz (Le Roux et al., 2007). If so, the age of LREE-enrichment may be similar to that of MORB-like melt metasomatism. At Mt. Briançon, this metasomatism is overprinted by metasomatic effects coming from migration of alkaline melts related to Cenozoic volcanism. As both a "metasomatic front" and metasomatism by alkaline melts lead to incompatible element enrichment in clinopyroxene, they are difficult to

distinguish in the studied rock population. The Group Ia lherzolites show various stages of transition between those of Group I and Group II and are characterized by spoon-like shapes of REE patterns.

Funding

This study was funded by Polish National Science Centre to MZM (research grant *Preludium* no. 2018/29/N/ST10/00259). SA was supported by the Deutsche Forschungsgemeinschaft (German Research Foundation) – Project number 467591567 (AU356/12). FIERCE is financially supported by the Wilhelm and Else Heraeus Foundation and by the Deutsche Forschungsgemeinschaft (DFG: INST 161/921-1 FUGG, INST 161/923-1 FUGG and INST 161/1073-1 FUGG), which is gratefully acknowledged. This is FIERCE contribution No. 166.

CRediT authorship contribution statement

Małgorzata Ziobro-Mikrut: Conceptualization, Data curation, Formal analysis, Funding acquisition, Investigation, Methodology, Project administration, Resources, Validation, Visualization, Writing – original draft, Writing – review & editing. **Jacek Puziewicz:** Conceptualization, Funding acquisition, Investigation, Methodology, Resources, Supervision, Validation, Visualization, Writing – original draft, Writing – review & editing. **Sonja Aulbach:** Conceptualization, Investigation, Methodology, Resources, Supervision, Validation, Writing – original draft, Writing – review & editing. **Mary-Alix Kaczmarek:** Data curation, Formal analysis, Investigation, Methodology, Resources, Supervision, Validation, Writing – original draft, Writing – review & editing. **Franz Kiraly:** Investigation, Resources.

Declaration of competing interest

The authors declare that they have no known competing financial interests or personal relationships that could have appeared to influence the work reported in this paper.

Acknowledgements

This study is a part of Ph.D. of MZM made under supervision of JP. We thank Arnaud Proietti for his help with EBSD analysis at the Centre de Microcaractérisation Raimond Castaing (Université Paul Sabatier, Toulouse). We are grateful to Prof. Theodoros Ntaflos (University of Vienna) for help when the microprobe analyses were collected and for inspiring discussions on the text.

Appendix A. Supplementary data

Supplementary data to this article can be found online at https://doi.org/10.1016/j.lithos.2024.107670.

References

Agranier, A., Lee, C.-T., 2007. Quantifying trace element disequilibria in mantle xenoliths and abyssal peridotites. Earth Planet. Sci. Lett. 257, 290–298.
Arai, S., 1994. Characterization of spinel peridotites by olivine–spinel compositional relationships: Review and interpretation. Chem. Geol. 113, 191–204.
Babuška, V., Plomerová, J., Vecsey, L., Granet, M., Achauer, U., 2002. Seismic anisotropy of the French Massif Central and predisposition of Cenozoic rifting and volcanism by Variscan suture hidden in the mantle lithosphere. Tectonics 21, 11-1-11-20.
Ben Ismaïl, W., Mainprice, D., 1998. An olivine fabric database: an overview of upper mantle fabrics and seismic anisotropy. Tectonophysics 296, 145–157.
Bestmann, M., Prior, D.J., 2003. Intragranular dynamic recrystallization in naturally deformed calcite marble: diffusion accommodated grain boundary sliding as a result of subgrain rotation recrystallization. J. Struct. Geol. 25, 1597–1613.
Brey, G., Köhler, T., 1990. Geothermobarometry in four-phase lherzolites II. New thermobarometers and practical assessment of existing thermobarometers. J. Petrol. 31, 1353–1378.
Cantagrel, J.-M., Prévot, M., 1971. Paléomagnétisme et âge potassium-argon des basaltes du Devès aux environs de Saint-Arcons-d'Allier (Massif Central, France). Comptes Rendus des Séances de l'Académie des Sciences France (B) 273, 261–264.
Chauvel, C., Jahn, B.-M., 1984. Nd-Sr isotope and REE geochemistry of alkali basalts from the Massif Central, France. Geochim. Cosmochim. Acta 48, 93–l10.
Davis, F., Tangeman, J., Tenner, T., Hirschmann, M., 2009. The composition of KLB-1 peridotite. Am. Mineral. 94, 176–180.
Dèzes, P., Schmid, S.M., Ziegler, P.A., 2004. Evolution of the European Cenozoic Rift System: interaction of the Alpine and Pyrenean orogens with their foreland lithosphere. Tectonophysics 389, 1–33.
Downes, H., Dupuy, C., 1987. Textural, isotopic and REE variations in spinel peridotite xenoliths, Massif Central, France. Earth Planet. Sci. Lett. 82, 121–135.
Downes, H., Reichow, M.K., Mason, P.R.D., Beard, A.D., Thirlwall, M.F., 2003. Mantle domains in the lithosphere beneath the French Massif Central: trace element and isotopic evidence from mantle clinopyroxenes. Chem. Geol. 200, 71–87.
Droop, G., 1987. A general equation for estimating Fe3+ concentrations in ferromagnesian silicates and oxides from microprobe analyses, using stoichiometric criteria. Mineral. Mag. 51, 431–435.
Franke, W., Cocks, R., Torsvik, T., 2017. The Palaeozoic Variscan oceans revisited. Gondwana Res. 48, 257–284.
Gale, A., Dalton, C.A., Langmuir, Ch.H., Su, Y., Schilling, J.-G., 2013. The mean composition of ocean ridge basalts. Geochem. Geophys. Geosyst. 14, 489–518.
Granet, M., Stoll, G., Dorel, J., Achauer, U., Poupinet, G., Fuchs, K., 1995. (Massif Central, France): new constraints on the geodynamical evolution from teleseismic tomography. Geophys. J. Int. 121, 33–48.
Gudfinnsson, G., Presnall, D., 2000. Melting behaviour of model lherzolite on the system CaO-MgO-Al_2O_3-SiO_2-FeO at 0.7-2.8 GPa. J. Petrol. 41, 1241–1269.
Harvey, J., Gannoun, A., Burton, K.W., Schiano, P., Rogers, N.W., Alard, O., 2010. Unravelling the effects of melt depletion and secondary infiltration on mantle Re–Os isotopes beneath the French Massif Central. Geochim. Cosmochim. Acta 74, 293–320.
Hidas, K., Garrido, C., Booth-Rea, G., Marchesi, C., Bodinier, J.-L., Dautria, J.-M., Louni-Hacini, A., Azzouni-Sekkal, A., 2019. Lithosphere tearing along STEP faults and synkinematic formation of lherzolite and wehrlite in the shallow subcontinental mantle. Solid Earth 10, 1099–1121.
Jean, M., Shervais, J., Choi, S.-H., Mukasa, S., 2010. Melt extraction and melt refertilization in mantle peridotite of the Coast Range ophiolite: an LA–ICP–MS study. Contrib. Mineral. Petrol. 159, 113–136.
Jennings, E., Holland, T., 2015. A simple thermodynamic model for melting of peridotite in the system NCFMASOCr. J. Petrol. 56, 869–892.
Jochum, K., Weis, U., Stoll, B., Kuzmin, D., Yang, Q., Raczek, I., Jacob, D.E., Stracke, A., Birbaum, K., Frick, D.A., Günther, D., Enzweiler, J., 2011. Determination of reference values for NIST SRM 610-617 glasses following ISO guidelines. Geostand. Geoanal. Res. 35, 397–429.
Jung, H., Karato, S.I., 2001. Water-induced fabric transitions in olivine. Science 293, 1460–1463.
Kaczmarek, M.-A., Jonda, L., Davies, H., 2015. Evidence of melting, melt percolation and deformation in a supra-subduction zone (Marum ophiolite complex, Papua New Guinea). Contrib. Mineral. Petrol. 170, 19.
Kaczmarek, M.-A., Bodinier, J.-L., Bosch, D., Tommasi, A., Dautria, J.-M., Kechid, S.A., 2016. Metasomatised mantle xenoliths as a record of the lithospheric evolution of the northern edge of the Ahaggar Swell, In Teria (Algeria). J. Petrol. 57, 345–382.
Katayama, I., Jung, H., Karato, S.I., 2004. New type of olivine fabric from deformation experiments at modest water content and low stress. Geology 32, 1045–1048.
Le Roux, V., Bodinier, J.-L., Tommasi, A., Alard, O., Dautria, J.-M., Vauchez, A., Riches, A.J.V., 2007. The Lherz spinel lherzolite: Refertilized rather than pristine mantle. Earth Planet. Sci. Lett. 259, 599–612.
Lenoir, X., Garrido, C., Bodinier, J.-L., Dautria, J.-M., 2000. Contrasting lithospheric mantle domains beneath the Massif Central (France) revealed by geochemistry of peridotite xenoliths. Earth Planet. Sci. Lett. 181, 359–375.
Liang, Y., Sun, Ch., Yao, L., 2013. A REE-in-two-pyroxene thermometer for mafic and ultramafic rocks. Geochimica et Cosmichimica Acta 102, 246–260.
Liotard, J., Briot, D., Boivin, P., 1988. Petrological and geochemical relationships between pyroxene megacrysts and associated alkali-basalts from Massif Central (France). Contrib. Mineral. Petrol. 98, 81–90.
Lorand, J.-P., Luguet, A., Alard, O., 2013. Platinum-group element systematics and petrogenetic processing of the continental upper mantle: a review. Lithos 164, 2–21.
Marchev, P., Arai, S., Vaselli, O., Costa, F., Zanetti, A., Downes, H., 2017. Metasomatic Reaction Phenomena from Entrainment to Surface Cooling: evidence from Mantle Peridotite Xenoliths from Bulgaria. J. Petrol. 58, 599–640.
Matusiak-Małek, M., Puziewicz, J., Ntaflos, T., Grégoire, M., Benoit, M., Klügel, A., 2014. Two contrasting lithologies in off-rift subcontinental lithospheric mantle beneath Central Europe – the Krzeniów, (SW Poland) case study. J. Petrol. 55, 1799–1828.
McDonough, W., Sun, S., 1995. The composition of the Earth. Chem. Geol. 120, 223–253.
Mehl, L., Hacker, B.R., Hirth, G., Kelemen, P.B., 2003. Arc-parallel flow within the mantle wedge: evidence from the accreted Talkeetna arc, south central Alaska. J. Geophys. Res. Solid Earth 108 (B8), 2375.
Meier, T., Soomro, R.A., Viereck, L., Lebedev, S., Behrmann, J.H., Weidle, C., Cristiano, L., Hanemannb, R., 2016. Mesozoic and Cenozoic evolution of the Central European lithosphere. Tectonophysics 692, 58–73.
Michibayashi, K., Mainprice, D., 2004. The role of pre-existing mechanical anisotropy on shear zone development within oceanic mantle lithosphere: an example from the Oman Ophiolite. J. Petrol. 45, 405–414.
Michon, L., Merle, O., 2001. The evolution of the Massif Central rift: spatio-temporal distribution of the volcanism. Bulletin de la Société Géologique de France 172 (2), 201–211.
Mercier, J.C., Nicolas, A., 1975. Textures and fabrics of upper-mantle peridotites as illustrated by xenoliths from basalts. J. Petrol. 16, 454–487.

Nicolas, A., Bouchez, J.L., Boudier, F., Mercier, J.-C., 1971. Textures, structures and fabrics due to solid state flow in some European lherzolites. Tectonophysics 12, 55–86.
Niu, Y., Langmuir, Ch., Kinzler, R., 1997. The origin of abyssal peridotites: a new perspective. Earth Planet. Sci. Lett. 152, 251–265.
Prior, J.D., Wheeler, J., Peruzzo, L., Spiess, R., Storey, C., 2002. Some garnet microstructures: an illustration of the potential of orientation maps and misorientation analysis in microstructural studies. J. Struct. Geol. 24, 999–1011.
Puziewicz, J., Matusiak-Małek, M., Ntaflos, T., Grégoire, M., Kaczmarek, M.-A., Aulbach, S., Ziobro, M., Kukuła, A., 2020. Three major types of subcontinental lithospheric mantle beneath the Variscan orogen in Europe. Lithos 362–363, 105467.
Puziewicz, J., Aulbach, S., Kaczmarek, M.-A., Ntaflos, T., Gerdes, A., Mazurek, H., Kukuła, A., Matusiak-Małek, M., Tedonkenfack, S., Ziobro-Mikrut, M., 2023. The origin and evolution of DMM-like lithospheric mantle beneath continents: Mantle xenoliths from the Oku Volcanic Group in the Cameroon Volcanic Line, West Africa. J. Petrol. 64, 1–25.
Rampone, E., Bottazzi, P., Ottolini, L., 1991. Complementary Ti and Zr anomalies in orthopyroxene and clinopyroxene from mantle peridotites. Nature 354, 518–520.
Roduit, N., 2007. JMicroVision: un logiciel d'analyse d'images pétrographiques polyvalent (PhD thesis). Université de Genève.
Rospabé, M., Ceuleneer, G., Benoit, M., Abily, B., Pinet, P., 2017. Origin of the dunitic mantle-crust transition zone in the Oman ophiolite: the interplay between percolating magmas and high-temperature hydrous fluids. Geology 45, 471–474.
Sawaguchi, T., 2004. Deformation history and exhumation process of the Horoman Peridotite Complex, Hokkaido, Japan. Tectonophysics 379, 109–126.
Schulmann, K., Edel, J.-B., Catalán, J.R.M., Mazur, S., Guy, A., Lardeaux, J.-M., Ayarza, P., Palomeras, I., 2022. Tectonic evolution and global crustal architecture of the European Variscan belt constrained by geophysical data. Earth-Sci. Rev. 234, 104195.
Skemer, P., Warren, J.M., Kelemen, P.B., Hirth, G., 2010. Microstructural and rheological evolution of a mantle shear zone. J. Petrol. 51, 43–53.
Streckeisen, A., 1976. To each plutonic rock its proper name. Earth Sci. Rev. 12, 1–33.
Sun, Ch., Liang, Y., 2014. An assessment of subsolidus re-equilibration on REE distribution among mantle minerals olivine, orthopyroxene, clinopyroxene, and garnet in peridotites. Chem. Geol. 372, 80–91.
Tedonkenfack, S., Puziewicz, J., Aulbach, S., Ntaflos, T., Kaczmarek, M.-A., Matusiak-Małek, M., Kukuła, A., Ziobro, M., 2021. Lithospheric mantle refertilization by DMM-derived melts beneath the Cameroon Volcanic Line – a case study of the Befang xenolith suite, Oku Volcanic Group. Cameroon. Contrib. Mineral. Petr. 176, 37.
Tilhac, R., Morishita, T., Hanaue, N., Tamura, A., Guotana, J.M., 2021. Systematic LREE enrichment of mantle harzburgites: the petrogenesis of San Carlos xenoliths revisited. Lithos 396-397, 106195.
Tommasi, A., Vauchez, A., 2015. Heterogeneity and anisotropy in the lithospheric mantle. Tectonophysics 661, 11–37.
Tommasi, A., Mainprice, D., Canova, G., Chastel, Y., 2000. Viscoplastic self-consistent and equilibrium-based modeling of olivine lattice preferred orientations: Implications for the upper mantle seismic anisotropy. J. Geophys. Res-Solid Earth 105, 7893–7908.
Tommasi, A., Vauchez, A., Godard, M., Belley, F., 2006. Deformation and melt transport in a highly depleted peridotite massif from the Canadian Cordillera: Implications to seismic anisotropy above subduction zones. Earth Planet. Sci. Lett. 252, 245–259.
Touron, S., Renac, C., O'Reilly, S., Cottin, J.-Y., Griffin, W., 2008. Characterization of the metasomatic agent in mantle xenoliths from Devès, (Massif Central, France) using coupled in situ trace-element and O, Sr and Nd isotopic compositions. In: Coltorti, M., Grégoire, M. (Eds.), Metasomatism in Oceanic and Continental Lithospheric Mantle. Geological Society, London, pp. 177–196. Special Publications 293.
Uenver-Thiele, L., Woodland, A.B., Seitz, H.M., Downes, H., Altherr, R., 2017. Metasomatic processes revealed by trace element and redox signature of the lithospheric mantle beneath the Massif Central, France. J. Petrol. 58, 395–422.
van Achterberg, E., Ryan, C.G., Jackson, S.E., Griffin, W.L., 2001. Data reduction software for LA-ICP-MS. In: Sylvester, P.J. (Ed.), Laser Ablation ICPMS in the Earth Sciences: Principles and Applications. Mineralogical Association of Canada, Short Course Series, 29, pp. 239–243.
Van der Wal, D., Bodinier, J., 1996. Origin of the recrystallization front in the Ronda peridotite by km-scale pervasive porous melt flow. Contrib. Mineral. Petrol. 122, 387–405.
Vanderhaeghe, O., Laurent, O., Gardien, V., Moyen, J.-F., Gébelin, A., Chelle-Michou, C., Couzinié, S., Villaros, A., Bellanger, M., 2020. Flow of partially molten crust controlling construction, growth and collapse of the Variscan orogenic belt: the geologic record of the French Massif Central. BSGF – Earth Sci. Bull. 191, 25.
Vernières, J., Godard, M., Bodinier, J.L., 1997. A plate model for the simulation of trace element fractionation during partial melting and magma transport in the Earth's upper mantle. J. Geophys. Res-Solid Earth 102, 24771–24784.
Wilson, M., Downes, H., 2006. Tertiary-Quaternary intra-plate magmatism in Europe and its relationship to mantle dynamics. Geological Society, London, "European Lithosphere Dynamics". Memoir 32, 147–166.
Wimmenauer, W., 1974. The alkaline province of Central Europe and France. In: Sørensen, H. (Ed.), The Alkaline Rocks. Wiley, London, pp. 286–291.
Witt-Eickschen, G., O'Neill, H.S., 2005. The effect of temperature on the equilibrium distribution of trace elements between clinopyroxene, orthopyroxene, olivine and spinel in upper mantle peridotite. Chem. Geol. 221, 65–101.
Wittig, N., Pearson, D.G., Baker, J.A., Duggen, S., Hoernle, K., 2010. A major element, PGE and Re-Os isotope study of Middle Atlas (Morocco) peridotite xenoliths: evidence for coupled introduction of metasomatic sulphides and clinopyroxene. Lithos 115, 15–26.
Woodland, A., Jugo, P., 2007. A complex magmatic system beneath the Devès volcanic field, Massif Central, France: evidence from clinopyroxene megacrysts. Contrib. Mineral. Petrol. 153, 719–731.
Yao, L., Sun, Ch., Liang, Y., 2012. A parameterized model for REE distribution between low-Ca pyroxene and basaltic melts with applications to REE partitioning in low-Ca pyroxene along a mantle adiabat and during pyroxenite-derived melt and peridotite interaction. Contrib. Mineral. Petrol. 164, 261–280.
Yoshikawa, M., Kawamoto, T., Shibata, T., Yamamoto, J., 2010. Geochemical and Sr–Nd isotopic characteristics and pressure–temperature estimates of mantle xenoliths from the French Massif Central: evidence for melting and multiple metasomatism by silicate-rich carbonatite and asthenospheric melts. In: Coltorti, M., Downes, H., Grégoire, M., O'Reilly, S.Y. (Eds.), Petrological Evolution of the European Lithospheric Mantle. Geological Society, London, pp. 153–175. Special Publications 337.
Zeyen, H., Novak, O., Landes, M., Prodehl, C., Driad, L., Hirn, A., 1997. Refraction-seismic investigations of the northern Massif Central, France. Tectonophysics 275, 99–117.
Ziegler, P.A., Dèzes, P., 2006. Crustal evolution of Western and Central Europe. Geological Society, London, "European Lithosphere Dynamics". Memoir 32, 43–56.